REPORT DOCUMENTATION PAGE

Form Approved
OMB No. 0704-0188

...E ONLY (Leave blank)	2. REPORT DATE	3. REPORT TYPE AND DATES COVERED
	April 10, 1995	Final Technical Report Due Jan 14, 1995

...SUBTITLE

...ıe Scale Structure of the Eurasian Crust and Upper ...ntle from High-Frequency Waves

5. FUNDING NUMBERS

AFOSR Contract # F49620-92-J0404

2309/AS

61102F

6. AUTHOR(S)

Prof. Thomas H. Jordan

7. PERFORMING ORGANIZATION NAME(S) AND ADDRESS(ES)

Department of Earth, Atmospheric, and Planetary Sciences
Massachusetts Institute of Technology
Cambridge, MA 02139

8. PERFORMING ORGANIZATION REPORT NUMBER

AFOSR-TR-95-0385

9. SPONSORING / MONITORING AGENCY NAME(S) AND ADDRESS(ES)

AFOSR
110 Duncan Avenue Suite B115
Bolling AFB, DC 20332-0001

10. SPONSORING / MONITORING AGENCY REPORT NUMBER

11. SUPPLEMENTARY NOTES

12a. DISTRIBUTION / AVAILABILITY STATEMENT

Approved for public release; distribution unlimited.

12b. DISTRIBUTION CODE

13. ABSTRACT *(Maximum 200 words)*

See Technical Summary, Page 1

Part 1: Science article (to be published)

Part 2: Journal of Geophysical Research article (to be published)

14. SUBJECT TERMS	15. NUMBER OF PAGES 70
	16. PRICE CODE

17. SECURITY CLASSIFICATION OF REPORT	18. SECURITY CLASSIFICATION OF THIS PAGE	19. SECURITY CLASSIFICATION OF ABSTRACT	20. LIMITATION OF ABSTRACT
UNCLASSIFIED	UNCLASSIFIED	UNCLASSIFIED	

Lehmann Discontinuity as the Base of an Anisotropic Layer Beneath Continents

James B. Gaherty and Thomas H. Jordan

Long-period surface-wave (*R1, G1*), body-wave (*S, SS, SSS*), and *ScS*-reverberation data have been inverted to obtain anisotropic structures along seismic corridors sampling Australia and the western Pacific. These models support the proposal that the Lehmann (L) discontinuity beneath stable continents represents a transition from an anisotropic lithosphere to a more isotropic material in the lower part of the continental tectosphere.

Lehmann (*1*) suggested that the behavior of refracted arrivals from North America and Europe at epicentral distances between 10° and 20° could be modeled by an increase in *P*-wave and *S*-wave speeds at a sharp lower boundary of the asthenospheric low-velocity zone (LVZ). Subsequent workers argued that this Lehmann (L) discontinuity occurs globally at an average depth near 220 km (*2,3*), and Dziewonski and Anderson (*4*) built it into the spherically averaged Preliminary Reference Earth Model (PREM). Solid-solid phase changes and chemical changes were ruled out as explanations (*5*), which led Hales (*3*) to conclude that this feature represents the base of a zone of partial melting, in agreement with Lehmann's basic hypothesis. However, L has not been detected in recent global stacks of long-period reflected waves (*6*), and, for a large area of the western Pacific and Australasia, it appears only on paths where the LVZ is weak or absent (*7*).

We have used new models of Australia and the western Pacific to test several alternative explanations of L that are based on the effects of seismic anisotropy. Leven et al. (*5*) first proposed that L might be related to shear-induced anisotropy in the subcontinental mantle. From a

---

Department of Earth, Atmospheric, and Planetary Sciences, Massachusetts Institute of Technology, Cambridge, MA 02139.

structural model of the Australian upper mantle derived from refracted *P* waves, they hypothesized that L is the upper boundary of a thin plate-decoupling zone underlying a nearly isotropic continental mechanical boundary layer (Fig. 1*a*). Revenaugh and Jordan (*7*) obtained upper-mantle reflectivity profiles from vertically propagating *ScS* reverberations that indicated a ~2% increase in vertical shear (*SV*) impedance at an L discontinuity with depths ranging from about 200 km along the northern Australian margin to over 250 km beneath the western Australian craton. Noting that the *SV* increase occurs near the level where some studies of refracted *SH* waves in continents have found a shear-velocity decrease (*8*), they proposed an alternative model where L marks the transition from an anisotropic mechanical boundary layer (MBL) to a more isotropic region below the MBL (Fig. 1*b*). Based on the apparent deepening of L towards the center of the western Australian craton, they speculated that this transition occurs at a critical temperature (near 1200°C) for the annealing of aligned textures in peridotites. They also pointed out that this horizon must be an internal feature of the continental thermal boundary layer, or tectosphere, whose thickness beneath cratons has been estimated to exceed 300 km (*9*).

Karato (*10*) accepted Revenaugh and Jordan's explanation of L as the rapid downward extinction of anisotropy, but he rejected their inference that such a feature could be maintained in a region of low deformation rate internal to the tectosphere. Instead, he proposed that L represents the transition from dislocation-controlled creep to diffusion-controlled creep in an actively deforming asthenosphere beneath the continental plate (Fig. 1*c*), and he reiterated Anderson's (*2*) suggestion that the tectospheric thicknesses obtained by Jordan (*9*) could be biased to high values owing to anisotropic effects.

The models we have used to test these hypotheses were derived from seismic waves propagating within two corridors, one continental and one oceanic, chosen to minimize along-path heterogeneities owing to tectonic complications (see inset map in Fig. 4). The first is an Australian path, connecting earthquakes in the New Britain/New Guinea convergence zone with station NWAO, largely sampling the Phanerozoic platforms and Precambrian cratons of the Australian continent. The second is a Pacific path (*11*), connecting earthquakes in the Tonga-Fiji seismic

zone with stations in Hawaii, traversing oceanic lithosphere with an average age of about 100 million years. The reflectivity structures for the two corridors are quite different (*12*). The seismic velocities and their gradients were constrained by frequency-dependent travel times of turning (*S*, *SS*, and *SSS*) and surface (R_1 and G_1) seismic phases measured from three-component, long-period seismograms using the isolation-filter techniques of Gee and Jordan (*13*). For the Australian corridor, we obtained approximately 800 observations for center frequencies from 10 to 45 mHz using 20 events with epicentral distances from 37° to 44°.

We inverted the frequency-dependent travel times and *ScS* reflectivity observations for a path-averaged, radially anisotropic model for each of the two corridors using an iterative, linearized perturbation scheme in which the elastic parameters, density, and discontinuity depths were adjusted to minimize a chi-squared measure of misfit (*14*). Our preferred Australia model (Fig. 2, Table 1) achieved a 90% reduction in data variance relative to the isotropic starting model (Fig. 3). It is characterized by an anisotropic mantle above an L discontinuity located at a depth of 252 ± 5 km, and an isotropic mantle below this boundary. The transition from an anisotropic to isotropic elastic structure at L is marked by an increase in *SV* impedance, consistent with the contrast observed for vertically propagating *ScS* reverberations, but a decrease in *SH* impedance. The latter feature of the Australia model yields an *SH* low-velocity zone similar to those inferred for other continental regions (*8*). The density and mean values of the elastic parameters are almost continuous across L (Fig. 4), as expected for a discontinuity that represents only a mechanical change in structure with no accompanying change in composition or phase.

We performed a number of inversions invoking a variety of prior constraints on the velocity distribution to test explicitly the hypotheses regarding the origin of L. The surface- and turning-wave data for the Australia corridor required significant radial anisotropy averaged over the upper 200 km of the mantle. Restricting the anisotropy to a thin (< 100 km) layer near a depth of 200 km, as in Fig. 1*a*, resulted in models that did not satisfy the Love-Rayleigh discrepancy and *SS* splitting observations. On the other hand, the *S* and *SS* splitting data constrained the magnitude of the anisotropy below L to be small (<1%), and inversions that allowed anisotropy in the layer

between the L and the 410-km discontinuities yielded no significant improvement in the fit to the data relative to the preferred model of Fig. 2. The Australian data are therefore consistent with L being the base of the anisotropic layer.

To discriminate between the hypotheses illustrated in Figs. 1*b* and 1*c*, we compared the shear-wave velocity structures derived for the Australian and Pacific corridors (Fig. 4). The shear-wave anisotropy of the latter is similar in magnitude to that of the former and extends below the G discontinuity into the oceanic LVZ, terminating at a weak discontinuity (unresolved by the *ScS* reverberation data) at a depth of 170 km (*11*). Below G, however, the mean shear velocities are lower in the oceanic case, and this difference persists to depths greater than 350 km. Attempts to satisfy both the Pacific and Australia data sets with models having similar shear velocities below 250 km were unsuccessful. Global tomographic models (*15*) and other regional studies (*16*) have demonstrated that differences between old continents and old oceans of this magnitude and depth are a global feature, indicative of a thick tectosphere beneath most Precambrian continental shields and platforms (*9, 17*). We infer that the average thickness of the continental tectosphere beneath the Australia corridor is greater than 300 km, and we conclude that L is a transition internal to the tectosphere (Fig. 1*b*), rather than a boundary within an actively deforming asthenosphere beneath the continental plate (Fig. 1*c*).

This result implies that the anisotropy above L is frozen in an MBL, or lithosphere, that forms the cold upper part of the tectosphere. The anisotropy is most plausibly related to the lattice preferred orientation of olivine, a highly anisotropic mineral known to dominate upper-mantle mineralogies (*18*). In the oceans, the fast axes of olivine grains tend to be horizontally aligned in the directions of the plate-scale flow associated with sea-floor spreading and are azimuthally coherent over large geographic distances. In the continents, however, the upper-mantle anisotropy appears to be inherited from major episodes of orogenic deformation (*19*). The superposition of many such episodes yields a fabric that varies on a much smaller geographical scale than the plate-tectonic flow field. In Australia, for example, lineaments in the gravity field associated with basement deformations have lateral scale lengths on the order of a few hundred kilometers (*20*). If

this is the appropriate scale length for the decorrelation of the lattice preferred orientation within the uppermost mantle beneath Australia, then waves propagating over epicentral distances of 30°–40° will average out the azimuthal variations, and the path-averaged structure can be approximated by a transversely isotropic effective medium. This inference is consistent with data from earthquakes in the Banda Sea to station CAN in southeast Australia (inset map in Fig. 4). Although these paths are orthogonal to those used in the inversion, we found that the Love-Rayleigh discrepancy and *SS* splitting measured for them were well fit by the Australia model.

As a further test, we developed stochastic models of upper-mantle heterogeneity in which orthorhombic peridotites have fast axes that are preferentially horizontal, but randomly oriented in azimuth (*21*). At low frequencies, such models yield transversely isotropic effective media, and their radial anisotropy can be made to match the Australia data using local anisotropies derived from mantle xenoliths brought to the surface by kimberlite pipes (*22*). At high frequencies, strong multiple scattering from the anisotropic heterogeneities couples the *SV* and *SH* wave fields, thereby mixing the shear-wave polarizations; this scattering may explain why the apparent S_n speeds observed in western Australia on short-period, vertical-component seismograms (*23*) are consistent with our *SH* velocities, not our *SV* velocities, and why paths sampling the upper 200 km of the northern margin of Australia do not show much *S*-wave splitting (*24*). The *ScS* reverberations, as well as the other data we used, cannot distinguish a sharp transition from one spread out over a depth interval of about 30 km (*25*). A transition zone of such width would explain why L is not consistently observed in studies of higher frequency converted waves (*26*).

The extinction of low-frequency polarization anisotropy at the L discontinuity can arise from either the disappearance of anisotropy at grain-size scales or the randomization of the fast-axis orientation out of the horizontal plane at regional scales. The first could be explained in terms of a kinetic boundary associated with long-term, thermally activated annealing of ancient deformation fabrics (*27*) or, alternately, by Karato's (*10*) rheological transition from dislocation to diffusion creep (although his proposal must be modified to generate an L discontinuity that is a relic feature frozen into the continental tectosphere). The second could be caused by a depth variation in the

types of strain fields active during tectospheric stabilization and any subsequent remobilization; for example, with deformations in the region above L involving nearly horizontal flows and those below L involving displacements with larger vertical components.

The L discontinuity is located near the maximum depth of equilibration observed for suites of kimberlite xenoliths from several continental cratons, which averages approximately 220 km (*28*). This equilibration level is interpreted to be the transition from slow diapiric upwelling of kimberlite magmas (or their precursors) (*29*) to much more rapid upward transport through a stronger lithosphere (*30*). The L discontinuity may thus correspond to the base of a mechanical boundary layer that overlies a more mobile, dynamically active part of the continental tectosphere. The apparent deepening of L beneath the western Australian craton (*7*) suggests that this rheological transition may be thermally controlled at 1200 to 1300°C. The transition also appears to correspond to a rapid increase in shear-wave attenuation observed at about this depth (*31*).

Our model provides an explanation for L in stable continental regions. Credible observations of discontinuities at depths of 180-220 km also have been made in island-arc (*32*) and marginal basin environments (*7*). Additional data will be needed to determine whether these discontinuities can be explained by the anisotropy-isotropy transition discussed here or require some other mechanism, such as the sharp lower boundary of a low-velocity zone. In this regard, we note that Revenaugh and Sipkin (*33*) have recently invoked both mechanisms to explain the multiplicity of discontinuities they observed in *ScS* reflectivity profiles crossing China and the Tibetian Plateau.

REFERENCES AND NOTES

1. I. Lehmann, *Ann. Géophys.* **15**, 93 (1959); *Geophys. J. R. Astron. Soc.* **4**, 124 (1961).
2. D. L. Anderson, *J. Geophys. Res.* **84**, 7555 (1979).
3. A. L. Hales, *Geophys. J. Int.* **105**, 355 (1991).
4. A. M. Dziewonski and D. L. Anderson, *Phys. Earth Planet. Inter.* **25**, 297 (1981).
5. J. H. Leven, I. Jackson, A. E. Ringwood, *Nature* **289**, 234 (1981).

6. P. M. Shearer, *Nature* **344**, 121 (1990).

7. J. Revenaugh and T. H. Jordan, *J. Geophys. Res.* **96**, 19781 (1991). This technique estimates the travel times down to and impedance contrasts across internal mantle reflectors from long-period, tangential-component recordings of multiple *ScS* reverberations. The ray paths of the reverberations are nearly vertical; hence, in the transversely isotropic model of mantle structure used here, the travel times and impedance contrasts are those defined in terms of the vertical shear (*SV*) velocities.

8. S. P. Grand and D. V. Helmberger, *Geophys. J. R. Astron. Soc.* **76**, 399 (1984); *Phys. Earth Planet. Inter.* **41**, 154 (1985).

9. T. H. Jordan, *Rev. Geophys.* 13, 1 (1975).

10. S.-I. Karato, *Geophys. Res. Lett.* **19**, 2255 (1992).

11. J. B. Gaherty, T. H. Jordan, L. S. Gee, submitted to *J. Geophys. Res.* (1995).

12. The Australian corridor was observed to have two reflectors in the mantle above 400 km, both characterized by impedance increases with depth: a H (Hales) discontinuity with an impedance contrast of $+4.9 \pm 0.9\%$ and a vertical *S*-wave reflection time of 28.4 ± 1.5 s, and an L discontinuity with a contrast of $+2.1 \pm 0.6\%$ and a reflection time of 115.6 ± 1.0 s. The Pacific corridor featured a G discontinuity with an impedance decrease of $-5.5 \pm 0.8\%$ and a reflection time of 29.7 ± 1.1 s, delineating the top of a relatively shallow (~60 km) *S*-wave low-velocity zone. Any G discontinuity in Australia and H or L discontinuity in the Pacific were below the detection threshold of the *ScS* reverberation data, which is about 1%. As Revenaugh and Jordan have noted, H may well be a global feature associated with the spinel-garnet facies boundary that is obscured by G on this and some other oceanic paths. The migrated *ScS* reverberation data also showed systematic differences in the locations and amplitudes of the transition-zone discontinuities for the two corridors, with the travel time between the 410-km and 660-km discontinuities being greater for Australia, implying lower temperatures in the transition zone beneath the continent. We utilized these observations by directly incorporating the observed impendance contrasts and vertical reflection times as data

in our inversions. We calculated the associated elements of the perturbation matrix using ray theory and plane-wave reflection coefficients.

13. L. S. Gee and T. H. Jordan, *Geophys. J. Int.* **111**, 363 (1992). In this technique, an observed seismogram is cross-correlated with a synthetic wave group (the isolation filter), and the cross-correlagram is windowed in the time domain (to reduce interference from other wave groups) and narrow-band filtered. To a good approximation, the resulting waveform is a Gaussian wavelet specified by four observables, which are functions of the narrow-band center frequency and functionals of the earth model. One of these generalized data functionals is the phase delay $\delta\tau_p$ of the observed wave group relative to the synthetic, the frequency-dependent travel-time residuals used in this study. Gee and Jordan give formulae for the Fréchet kernels of the phase-delay functional as a sum over traveling modes that include the first-order effects of interference from other arrivals. This methodology allowed us to consistently measure and interpret phase delays from complex wave groups like *SS* and *SSS* on three-component seismograms without resorting to high-frequency or isolated-phase approximations.

14. In our models, the effective elasticity tensor was assumed to be transversely isotropic (radially anisotropic), parameterized according to the PREM conventions (*4*): v_{PH} and v_{PV} are the speeds of *P* waves propagating horizontally and vertically, respectively; v_{SH} is the speed of a horizontally propagating, transversely polarized shear wave; v_{SV} is the speed of a shear wave propagating either horizontally with a vertical polarization, or vertically with horizontal polarization; and η governs the variation of the shear and compressional wave speeds at oblique propagation angles. Between discontinuities, these five elastic parameters and the mass density ρ were taken to be linear functions of depth.

15. J. H. Woodhouse and A. M. Dziewonski, *J. Geophys. Res.* **89**, 5953 (1984); W.-J. Su, R. L. Woodward, A. M. Dziewonski, *J. Geophys. Res.* **99**, 6945 (1994).

16. S. P. Grand and D.V. Helmberger, *J.Geophys. Res.* **89**, 11465 (1984); A. L. Lerner-Lam and T. H. Jordan, *J. Geophys. Res.* **92**, 14007 (1987).

17. T. H. Jordan, in *Journal of Petrology, Special Volume*, M. A. Menzies, K. G. Cox, Eds. (Oxford University Press, Oxford, 1988), pp. 11-37; T. H. Jordan, A. L. Lerner-Lam, K. C. Creager, in *Mantle Convection*, W. R. Peltier, Ed. (Gordon and Breach, New York, 1989), pp. 98-201.

18. L. H. Estey and B. J. Douglas, *J. Geophys. Res.* **91**, 11393 (1986); A. Nicolas and N. I. Christensen, *Rev. Geophys.* **25**, 111 (1987).

19. P. G. Silver and W. W. Chan, *J. Geophys. Res.* **96**, 16429 (1991); P. G. Silver and S. Kaneshima, *Geophys. Res. Lett.* **20**, 1127 (1993).

20. See figure 1.1 of R. W. R. Rutland in *Precambrian of the Southern Hemisphere*, D. R. Hunter, Ed. (Elsevier, Amsterdam, 1981), pp. 1-32.

21. T. H. Jordan and J. B. Gaherty, in *Proceedings of the 16th Annual Seismic Research Symposium*, J. J. Cipar, J. F. Lewkowicz, J. M. McPhetres, Eds. (Phillips Laboratory Technical Report PL-TR-94-2217, Hanscom A.F.B., MA, 1994), pp. 189-195. In these stochastic models, the spatial distribution of orientations is scale-invariant (fractal) up to some horizontal correlation length (outer scale) l_h and some vertical correlation length l_z. We distinguish two cases: equidimensional stochastic heterogeneity, with an aspect ratio near unity ($a \equiv l_h/l_z \sim 1$), and a stochastic laminate, with a large aspect ratio ($a >> 1$). For wavelengths much greater than l_z and propagation distances much greater than l_h, the effective media in both cases are transversely isotropic with elastic properties that are independent of l_h and l_z.

22. The local anisotropy measured in mantle xenoliths ranges from 3 to 8% [(*34*); N. I. Christensen, personal communication, 1994]. The relative shear-wave anisotropy of 3% obtained for Australia can be made consistent with these somewhat larger values by invoking dispersion of the fast (a) axis of olivine out of the horizontal plane.

23. J. R. Bowman and B. L. N. Kennett, *Bull. Seism. Soc. Am.* **83**, 25 (1993).

24. C. Tong, O. Gudmundsson, B. L. N. Kennett, *J. Geophys. Res.* **99**, 15783 (1994).

25. See figure 4 of J. Revenaugh and T. H. Jordan [*J. Geophys. Res.* **96**, 19763 (1991)].

26. G. Bock, *Geophys. J.* **94**, 73 (1988).

27. A. M. Boullier and A. Nicolas, *Phys. Chem. Earth* **9**, 467 (1975); ref. *34*.

28. A. A. Finnerty and F. R. Boyd, in *Mantle Xenoliths*, P. H. Nixon, Ed. (Wiley-Interscience, Chichester, 1987), pp. 381-402.

29. H. W. Green and Y. Gueguen, *Nature* **249**, 617 (1974).

30. D. A. Spence and D. L. Turcotte [*J. Geophys. Res.* **95**, 5133 (1990)] argue that kimberlites erupt via magma fracture, which implies a mechanically competent lithosphere extending to their depths of origin.

31. O. Gudmundsson, B. L. N. Kennett, A. Goody, *Phys. Earth Planet. Inter.* **84**, 207 (1994).

32. J. E. Vidale and H. M. Benz, *Nature* **356**, 678 (1992).

33. J. Revenaugh and S. A. Sipkin, *J. Geophys. Res.* **99**, 21911 (1994).

34. D. Mainprice and P. G. Silver, *Phys. Earth Planet. Inter.* **78**, 257 (1993).

35. We thank L. Gee and S. Shapiro for assistance in code development during the early stages of this project and P. Shearer for a helpful review of the manuscript. This research was sponsored by the Air Force Office of Scientific Research under grant F49620-92-J0404.

FIGURE CAPTIONS

Fig. 1. Schematic cross-sections of the continental upper mantle illustrating three competing hypotheses regarding the relationship of the L discontinuity to upper-mantle anisotropy. (A) Model of Levin et al. (*5*), derived from an analysis of *P*-wave refraction data in northern Australia, which indicated a high-velocity zone in the depth interval 190-225 km. They interpreted this feature to be an expression of the horizontal alignment of olivine crystals by the present-day northward motion of the Australian continent; L thus defines the transistion between the base of the continental plate (tectosphere) and this narrow shear decoupling zone. (B) Model of Revenaugh and Jordan (*7*), where L is the base of an anisotropic mechanical boundary layer overlying a nearly isotropic layer that forms the lower part of a thick (> 300 km) continental tectosphere. The drop in the magnitude of the polarization anisotropy across this narrow (< 30 km) transition causes an increase in the vertical wave speed and a decrease in the horizontal wave speed, but no appreciable change in their isotropic average. (C) Model of Karato (*12*), who proposed that L is the transition from dislocation-dominated creep (which induces anisotropy in olivine) to diffusion-dominated creep (which does not) in an actively deforming asthenosphere beneath a thin (< 200 km) continental tectosphere. Thickness of the shear decoupling zone is not constrained in either model (B) or (C). Diagrams labeled $\Delta v/v$ show schematically the perturbations to the vertical (*solid line*) and horizontal (*dashed line*) wave speeds relative to the isotropic average; *left* is for model (A), *right* is for both models (B) and (C).

Fig. 2. Transversely isotropic model of the upper mantle for the Australia (New Britain-NWAO) corridor, obtained from the inversion of the 797 frequency-dependent travel times summarized in Fig. 3 and the 13 *ScS* reflectivity observations of ref. 7. From left to right, the lines represent the anisotropic parameter η, density ρ, *S*-wave velocities v_{SV} and v_{SH}, and *P*-wave velocities v_{PV} and v_{PH}. Tick marks show the locations of the Mohorovičić (M), Hales (H), and Lehmann (L) discontinuities; other first-order discontinuities are located at 406, 499, and 659 km. The model is radially anisotropic with differing horizontal (*dashed lines*) and vertical (*solid lines*) velocities between the M and L discontinuities, and is isotropic elsewhere. The relative *S*-wave and *P*-wave

anisotropies are comparable, averaging 3.3 ± 0.5% and 3.7 ± 1.5%, respectively, although the former is much better determined by the data than the latter. The model is identical to PREM (*4*) below 860 km.

Fig. 3. Average phase delays $\delta\tau_p$ for the Australia corridor referenced to an isotropic starting model and plotted against circular frequency for surface waves (*top panel*), *SS* waves (*middle*), and *S* waves (*bottom*). Points with standard errors are averages of measurements for each seismic phase from vertical (*squares*) and transverse (*circles*) seismograms, summarizing the 797 frequency-dependent travel times used in the inversions; solid and dashed lines are corresponding averages computed for the Australia model of Fig. 2. The existence of polarization anisotropy at shallow depths in the Australian upper mantle is indicated by the large Love-Rayleigh discrepancy (> 20 s), moderate *SS*-wave splitting (~ 10 s), and small *S*-wave splitting (< 4 s).

Fig. 4. Comparison of shear-wave structures for the Australian and Pacific corridors. Mean shear-wave speeds are plotted for Pacific (*dashed-dot line*) and Australia (*solid line*) in the center diagram, and the anisotropic velocity perturbations relative to these mean velocities are displayed on the left and right, respectively. The contrasts in velocities and discontinuity structure inferred above a depth of about 350 km are evidence for a thick tectosphere beneath Australia. *Inset map* shows earthquakes and seismic stations that define the two corridors. New Britain (*stars*) events recorded at NWAO were used to generate the Australia model, while Tonga events (*dots*) recorded at HON and KIP were used for the Pacific model. Banda Sea earthquakes (*crosses*) recorded at CAN were used to test for azimuthal variations in anisotropy beneath Australia (see text).

Table 1. Upper-mantle model for Australia. Parameters are linearly interpolated between each discontinuity. Model is identical to PREM (*4*) through the remainder of the lower mantle and core.

Depth, km	v_{PH}, km/s	v_{PV}, km/s	v_{SH}, km/s	v_{SV} km/s	ρ, g/cm^3	η
0	6.05	6.05	3.62	3.62	2.85	1.00
30	6.05	6.05	3.62	3.62	2.85	1.00
30	8.15	8.00	4.40	4.28	3.30	0.90
54	8.15	8.00	4.40	4.28	3.30	0.90
54	8.52	8.23	4.68	4.56	3.40	0.90
252	8.61	8.28	4.70	4.52	3.44	0.90
252	8.45	8.45	4.63	4.63	3.45	1.00
406	8.88	8.88	4.80	4.80	3.58	1.00
406	9.31	9.31	5.07	5.07	3.69	1.00
499	9.64	9.64	5.19	5.19	3.85	1.00
499	9.67	9.67	5.23	5.23	3.88	1.00
659	10.21	10.21	5.58	5.58	4.00	1.00
659	10.72	10.72	5.94	5.94	4.21	1.00
861	11.21	11.21	6.28	6.28	4.50	1.00

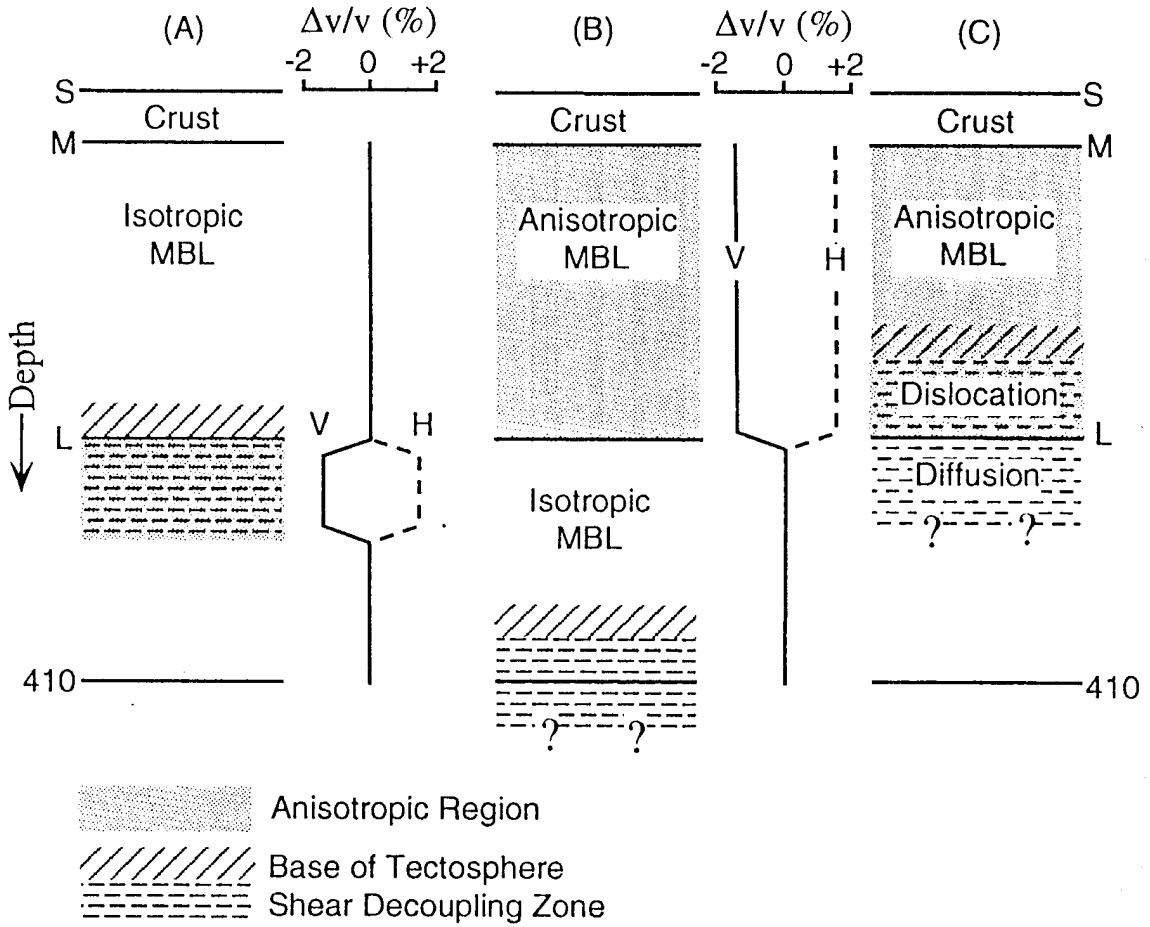
(A)
Δv/v (%)
-2 0 +2
S
Crust
M
Isotropic
MBL
Depth
L
V
H
410
(B)
Δv/v (%)
-2 0 +2
Crust
Anisotropic
MBL
V
H
Isotropic
MBL
?
?
(C)
S
Crust
M
Anisotropic
MBL
Dislocation
L
Diffusion
?
?
410
Anisotropic Region
Base of Tectosphere
Shear Decoupling Zone

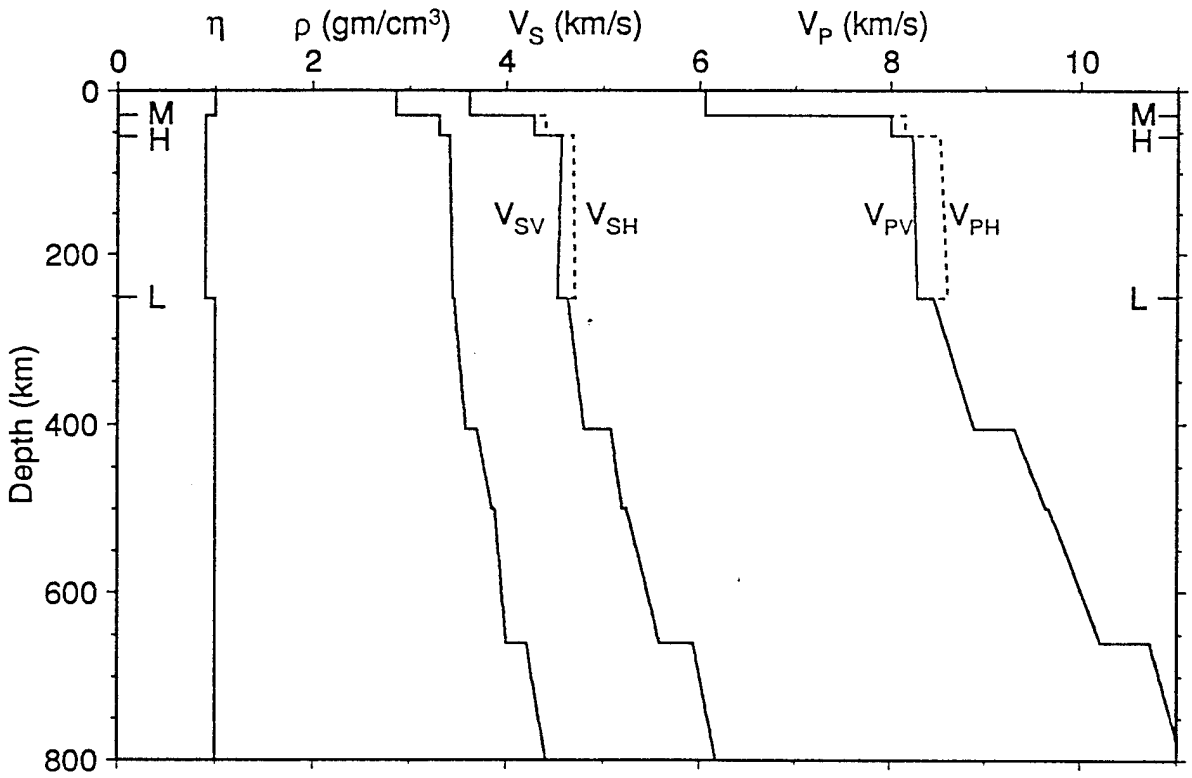
η
ρ (gm/cm3)
VS (km/s)
VP (km/s)
0
2
4
6
8
10
0
200
400
600
800
Depth (km)
M
H
L
VSV
VSH
VPV
VPH
M
H
L

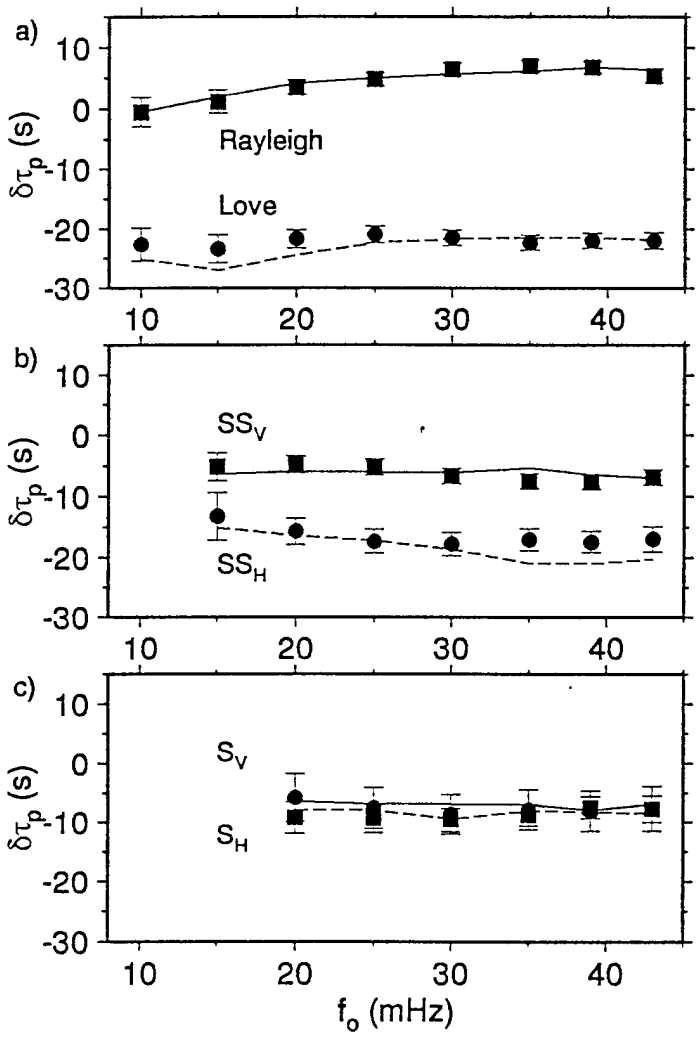
a)
b)
c)
Rayleigh
Love
SS$_V$
SS$_H$
S$_V$
S$_H$
$\delta\tau_p$ (s)
10
0
-10
-20
-30
10
20
30
40
f_o (mHz)

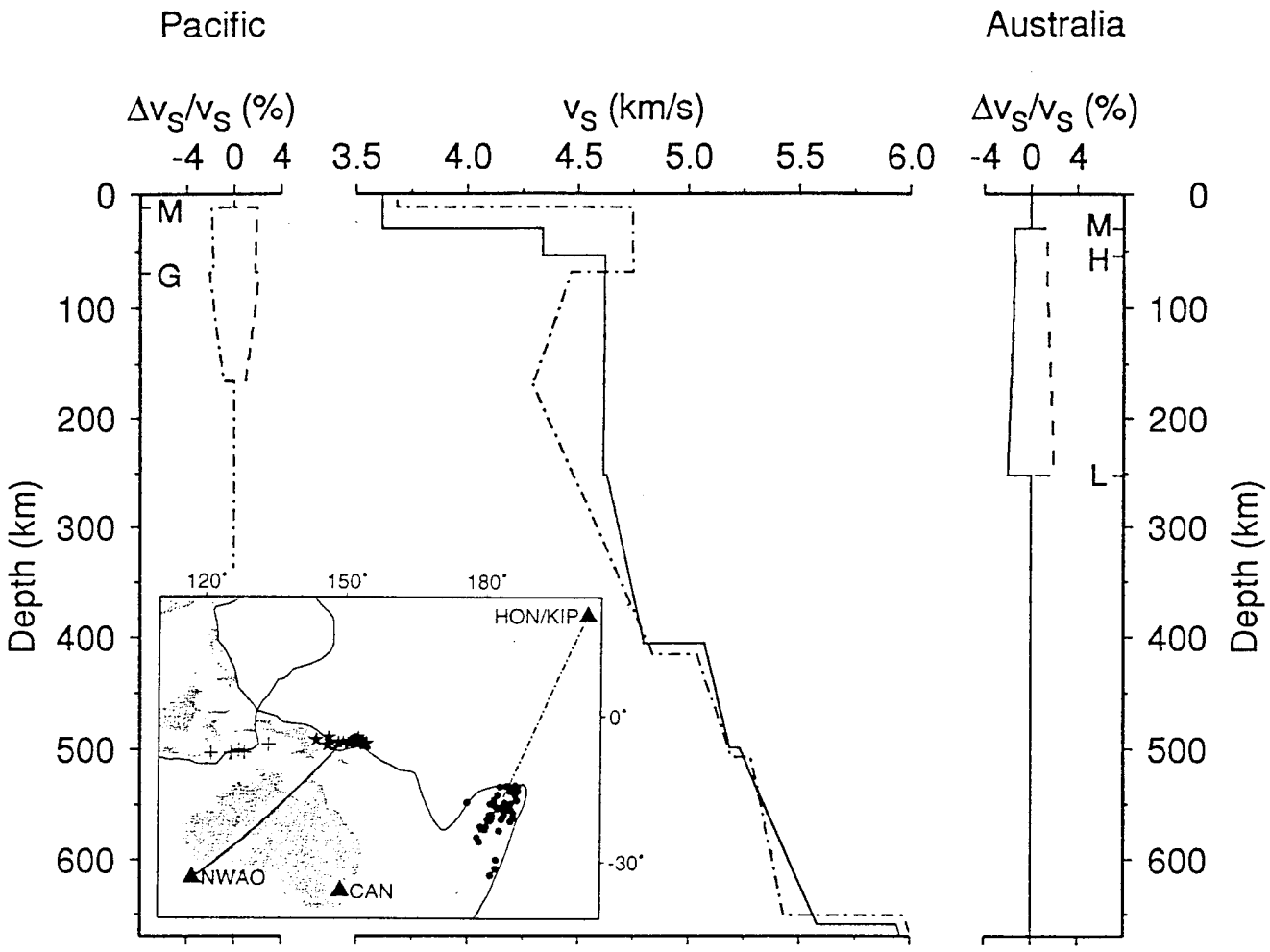
Pacific
Australia
$\Delta v_S/v_S$ (%)
v_S (km/s)
$\Delta v_S/v_S$ (%)
-4 0 4
3.5 4.0 4.5 5.0 5.5 6.0
-4 0 4
0
100
200
300
400
500
600
Depth (km)
M
G
M
H
L
120°
150°
180°
HON/KIP
0°
-30°
NWAO
CAN

Seismic Structure of the Upper Mantle in a Western Pacific Corridor

JAMES B. GAHERTY AND THOMAS H. JORDAN
Department of Earth, Atmospheric, and Planetary Sciences, MIT

LIND S. GEE
Seismographic Station, University of California, Berkeley

Abstract. We investigate the nature of seismic anisotropy in the western Pacific upper mantle by inverting data from two new seismic techniques that provide increased vertical resolution of upper mantle structure. The analysis of *ScS* reverberations provides estimates of the travel time to and impedance contrasts across all significant upper mantle and transition zone discontinuities, establishing a precise layered framework for upper mantle structure. The measurement of frequency-dependent phase delays of a general class of three-component turning and surface waves such as *S, SS, SSS, R1*, and *G1* are used to constrain the velocity structure within this layered framework. Both techniques utilize path average approximations to determine one-dimensional structure within tectonically "pure" corridors. In this paper we invert an extensive data set (15 *ScS*-reverberation data plus 1500 frequency-dependent travel times from 233 waveforms) that samples the upper mantle beneath 100-125 Ma oceanic lithosphere between the Tonga-Fiji seismic zone and Hawaii. The damped, linearized inversion employs prior constraints on the expected distribution of mineralogical observables such as bulk sound velocity and density, as well as on the allowable distribution of polarization anisotropy. Our final model, dubbed PA5, is characterized by a high velocity, anisotropic lithosphere, bounded at 69 km depth by a large (negative) Gutenburg (G) discontinuity; a distinct low velocity zone with anisotropic structure extending to 166 km depth; no significant Lehmann (L) discontinuity; an isotropic, steep-gradient region between 166 km and 415 km depth; and transition zone discontinuities at 415 km, 507 km, and 651 km depth. These results indicate that oceanic upper mantle probably contains anisotropic structure that is both locked into the lithosphere during plate formation, and actively being maintained by current dynamic flow in the asthenosphere. Similarity in anisotropic signature between the Tonga-Hawaii path and an alternative path in the western Pacific indicates that the lithospheric regime predominates, and that any dynamic flow alignment does not coincide with current plate motion. The depth of transition between these regimes is ambiguous. The thickness of the seismic lithosphere is well constrained; hence, the discrepancy between seismic and thermal lithospheric thicknesses must be incorporated into models of oceanic upper mantle.

INTRODUCTION

Over the last decade, remarkable advances have been made in mapping lateral variations in the Earth's seismic velocity structure. Three-dimensional tomographic models provide maps of shear and compressional velocity variations in the crust, mantle, and core available on global and regional scales, generating new insight into the structure, composition, and dynamics of the Earth's interior. Such models do have short-comings, however, primarily due to the limited resolution of seismic data sets and constraints on the number of parameters that realistically can be included in such models. As a result, point-sample, path-average, or regionalized modeling remain the most fruitful approaches to analyzing important features such as seismic discontinuities, anisotropy, and radial gradients in shear and compressional velocities. These features display dramatic variability over relatively short scale lengths, with the variability often correlating with surface tectonics. For example, discontinuities reflect variations in mantle temperature, composition, and phase that correlate with plate structure and dynamic processes such as subduction [*Revenaugh and Jordan*, 1989, 1991a-c; *Shearer and Masters*, 1992; *Vidale and Benz*, 1992], while anisotropy illuminates tectonic history [*Hess*, 1964; *Forsyth*, 1975; *Shearer and Orcutt*, 1986; *Gee and Jordan*, 1988; *Nishimura and Forsyth*, 1989; *Silver and Chan*, 1991] and current dynamic flow [*Vinnik et al.*, 1992; *Gao et al*, 1994; *Russo and Silver*, 1994]. Radial gradients constrain variations in temperature and mineralogical structure that again appear to correlate with plate structure [*Grand and Helmberger*, 1984a; *Lerner-Lam and Jordan*, 1987]. Many of these inferences cannot be drawn from the current generation of three-dimensional tomographic models.

In this paper we initiate a new generation of regional studies that jointly model variable discontinuities and anisotropic S- and P- velocities in the upper mantle, by applying two complementary seismic analysis techniques that provide increased vertical resolution of upper-mantle structure. We start with the results of *Revenaugh and Jordan* [1991a-c], who employ *ScS*-reverberations to identify, locate and measure the impedance contrasts of upper-mantle discontinuities for several corridors crossing a variety of tectonic environments in the southwest

Pacific and Australasia. The resulting vertical travel times and impedance contrasts establish a precise layered framework for corridor-specific upper mantle velocity models. Velocities (and anisotropy) within this framework are constrained by frequency-dependent travel times of turning (*S*, *SS* and *SSS*) and surface (R_1 and G_1) seismic phases measured from three-component, long-period seismograms using the isolation filter techniques of *Gee and Jordan* [1992]. We invert jointly these two data sets for layered, path-average, radially anisotropic models in which discontinuity depths, velocities, and linear velocity gradients are allowed in vary in each layer. We restrict our analysis to narrow corridors to focus on particular tectonic environments with minimal interference from structural complexities; three-dimensional variability can then be assessed by contrasting models from various corridors. In this study, we analyze a purely oceanic path extending from the Tonga-Fiji seismic zone to stations in Hawaii (Figure 1). While the restriction of our model parameterization to spherical symmetry averages out three-dimensional velocity and anisotropy information, it allows us to generate regional seismic models that better characterize variability in radial anisotropy, discontinuities, and radial gradients than global three-dimensional parameterizations. Our primary result is a regional seismic model that represents the structure of 100-125 Ma Pacific lithosphere and upper mantle. The presence of a thin seismic lithosphere (lid), a distinct low-velocity zone (LVZ) with a sharp discontinuity above but no discontinuity below, and high gradients between 200 km and 400 km depth are all features of our model that are difficult to infer from more general 3-D interpretations [e.g. *Su et al.*, 1994]. Our three-component analysis requires that we invert for all 6 independent parameters in our transversely isotropic model, and we include laboratory data on mineral elasticity in our inversion to ensure self-consistent *S*, *P*, and density models.

In generating our regional seismic model, we evaluate the depth extent of anisotropic structure in western Pacific upper mantle by utilizing an inversion scheme incorporating prior constraints on the model distribution [e.g. *Tarantola*, 1987]. For example, can the surface- and body-wave data be satisfied by an anisotropic model in which the anisotropy is confined to the seismic lithosphere, or does the data require an additional component of anisotropy in the low-

velocity zone below the lid? We thereby evaluate a number of models with variable depth extent of the anisotropy, rather than simply assuming a depth distribution [*Dziewonski and Anderson*, 1981; *Regan and Anderson*, 1984]. In addition, we allow the anisotropy to terminate discontinuously if the data prefer, rather than enforcing a smooth distribution [*Nishimura and Forsyth*, 1989; *Montagner and Tanimoto*, 1991]. Discontinuities in velocity structure imply rapid changes in mechanical, phase, or compositional structure, and a discontinuity appears to represent a lower boundary for anisotropic structure in another region [*Gaherty and Jordan*, 1995]; we test for similar behavior here. The firm establishment of the depth extent of anisotropic structure and it's correlation with the background discontinuity and velocity structure lead to new inferences of the mechanical state of oceanic upper mantle.

We start our analysis by presenting our observations, including a description of the observed discontinuity structure and a summary of the isolation filter techniques. We then describe the inversion procedure, rationalizing our model parameterization and our selected *a priori* constraints. Our results include the preferred model and its fit to the data, along with a discussion of less acceptable alternative models. An introductory analysis of other Pacific paths sheds light on the lateral length scales of the anisotropic structure. We discuss the implications of our model for Pacific upper mantle thermal and rheological structure. In other work we compare these results to anisotropic models from other tectonic regimes, including cratonic western Australia [*Gaherty and Jordan*, 1995], thereby improving our understanding of the Earth's upper mantle.

TONGA/FIJI-TO-OAHU CORRIDOR

We analyze data sampling an oceanic path between the Tonga-Fiji seismic zone and the island of Oahu, Hawaii (Figure 1). Magnetic lineations indicate that this corridor crosses oceanic lithosphere with ages between 100-125 Ma, and it has a bathymetric depth of ~5 km and sediment thickness of ~200 meters [*Ludwig and Houtz*, 1979]. The corridor is situated west of the Pacific Superswell [*McNutt and Judge*, 1990], although it crosses the eastern margin of the Darwin Rise (in particular the Line Islands), a region of abnormally proficient Cretaceous volcanism [*Menard*,

1984]. The current plate motion relative to a hot-spot reference frame is roughly perpendicular to the path [*Gripp and Gordan*, 1991].

Much is already known about the seismic structure of this corridor, primarily via analyses of multiple *ScS* [*Sipkin and Jordan*, 1976, 1980; *Gee*, 1994] and *ScS* reverberations [*Revenaugh and Jordan*, 1987, 1989, 1991a-d]. Multiple *ScS* provides whole mantle travel time and Q estimates, and reverberations provide impedance contrast and vertical travel times for internal mantle discontinuities, as well as Q estimates for upper- and lower-mantle layers. The path average structure inferred from these observations is summarized in Figure 2. The reflectivity profile is characterized by a Gutenburg (G=lid/LVZ, near 70 km depth), 410-km, 520-km, and 660-km discontinuities. Notably absent is evidence for the Hales discontinuity (~50 km depth), perhaps because it is obscured by the large G [*Revenaugh and Jordan*, 1991c]. Also missing is the Lehmann discontinuity (~220 km depth), which is ubiquitously observed on paths with a significant continental component [*Revenaugh and Jordan*, 1991c]. The apparent depths are estimates only; the observed vertical travel times represent the data included in our study. The whole mantle Q_{ScS} estimate is 169 ± 30; this is partitioned into $Q_{UM} = 82 \pm 18$ and $Q_{LM} = 231 \pm 60$ [*Revenaugh and Jordan*, 1987, 1991a]. As we expect there to be a significant Q contrast between the lid, LVZ, and transition zone, we further partition Q_{UM} into $Q_{LID} = 150$, $Q_{LVZ} = 30$, and Q_{TZ}=150; this assumption is validated by forward modeling. These Q values are maintained throughout our study.

Lateral variations in velocity structure have been observed in this region; tomographic models [e.g. *Zhang and Tanimoto*, 1993; *Su et al.*, 1994] typically show low-velocity regions (~ 1% slow) in the upper mantle beneath both Tonga/Fiji and Hawaii, with a relatively fast region in between. In addition, travel times of multiple-*ScS* phases show large along-path variations [*Sipkin and Jordan*, 1980; *Gee*, 1994] that probably arise (in part) from velocity anomalies in the upper mantle. These examples of lateral heterogeneity point out the limitations in our path-average approach. However, as demonstrated below, there is much we can learn by determining an average structure for this corridor.

DATA ANALYSIS

We initiate our analysis by incorporating the reflectivity results of *Revenaugh and Jordan* [1991a,c], specifically the vertical travel times (t_V) to and shear impedance (R_O) contrasts across discontinuities. Shear impedance is defined as

$$R_o = \frac{\rho^- v_{sv}^- - \rho^+ v_{sv}^+}{\rho^- v_{sv}^- + \rho^+ v_{sv}^+}$$

where ρ_{sv}^- and v_{sv}^- are the density and SV velocity just below a given discontinuity, respectively, and ρ_{sv}^+ and v_{sv}^+ are the velocity and density above the discontinuity. Table 1 presents t_V and R_O for the Moho, G, 410-km, 520-km, and 660-km discontinuities. The observed discontinuity structure is roughly compatible with model PA2 of *Lerner Lam and Jordan* [1987], which is constructed to fit Rayleigh waves from the western Pacific, and using it as a starting model for our inversion, we calculate residuals of the *ScS*-reverberation observations relative to it. G is observed to be shallower and somewhat larger in amplitude (more negative) than in PA2, while the observed 410-km and 660-km discontinuities appear deeper and shallower, respectively. PA2 has an L discontinuity with a positive impedance contrast, and although no discontinuity is observed near this depth on this path, it is convenient to include a second-order discontinuity near this depth to allow for two distinct gradients between G and 410 km. We interpret the lack of an observed L in terms of a discontinuity with R_O = 0.0 (with appropriate observational error) and an unconstrained vertical travel time. Conversely, PA2 does not include the 520-km discontinuity observed on this path, and a positive impedance residual is calculated for a depth approximately correct for the observed travel time. The partial derivatives of these data with respect to our model parameters are straight-forward to calculate from ray theory and plane-wave reflection coefficients[*Revenaugh and Jordan*, 1989].

We complement these data with frequency-dependent phase delays of surface, multiply-reflected (*SS, SSS*), and direct (*S*) body waveforms extracted from 3-component, long-period seismograms of 55 earthquakes in the Tonga-Fiji region recorded at the DWWSSN station HON and the jointly operated IRIS/USGS-Geoscope station KIP (Figure 1 and Table 2). The recorded

seismograms are rotated into the tangential-radial-vertical coordinate system and low-passed with a zero-phase filter with a corner at 45 mHz. The earthquakes are all of moderate size ($M_W < 6.4$), minimizing unmodeled source effects, and range in source depth from 10 km to 663 km and epicentral distance from 39°-58°, providing excellent sampling of the upper mantle. Evidence of anisotropy can be observed directly from the seismograms (Figure 3). While the initial phase of the observed Rayleigh wave is reasonably well matched by PA2, the observed Love wave is clearly much faster than the synthetic, and the magnitude of the misfit indicates that the difference cannot be rectified by an isotropic model. Likewise, *SSS* observations from a deep focus event (Figure 4) shows clear evidence of shear wave splitting, with SSS_H advanced by approximately 6 s relative to SSS_V.

We analyze these data using the Generalized Seismological Data Functional (GSDF) methodology of *Gee and Jordan* [1992], which makes use of the ability to calculate accurate synthetic seismograms in order to isolate a general waveform on the seismogram and calculate differential phase delays for that waveform at discrete frequency intervals relative to a reference model, in this case PA2. Briefly, the processing consists of (1) creating an "isolation filter", i.e. a synthetic seismogram of a chosen wave group calculated by performing a weighted sum of eigenfunctions for a subset of modes selected by phase velocity, group velocity, and/or other characteristics; (2) cross-correlating the isolation filter with both the observed and complete synthetic seismograms, creating two broad-band correlation functions; (3) windowing the correlation functions in the time domain to reduce interference with other wave groups; (4) filtering the windowed correlation functions in several discrete narrow-band windows in the interval $10 \leq f_o \leq 45$ mHz; and (5) extracting four time-like quantities (phase delay $\delta\tau_p$, group delay $\delta\tau_g$, attenuation delay $\delta\tau_q$, and amplitude delay $\delta\tau_a$) relative to the synthetic at each f_o using a Gaussian wavelet approximation. These quantities completely describe the behavior of the observed waveform relative to the model-predicted behavior, including correction for interference from unmodeled wavegroups. In this analysis we focus on the phase delay ($\delta\tau_p$). By performing a weighted sum of the modal Fréchet kernels [*Anderson and Dziewonski*, 1982; *Woodhouse and*

Dziewonski, 1984] for the subset of modes selected in each isolation filter, we can calculate the partial derivative kernels associated with each $\delta\tau_p$ observation for the six parameters of a radially anisotropic model (v_{SH}, v_{SV}, v_{PH}, v_{PV}, η, and ρ) and accompanying discontinuities, leading to a straight-forward solution to the linearized inverse problem for an improved model. *Gee and Jordan* [1992] provide a detailed description of the GSDF procedure.

This process is depicted for a vertical-component *SSS* phase in Figure 5. Figure 5a displays the data, a full synthetic seismogram, and an isolation filter formed by summing the eigenfunctions for all excited modes with group velocities of 4.10-4.30 km/s and phase velocities less than 8 km/s; this process isolates the phase in time and eliminates contributions from core-interaction phases. Phase delays (frequency-dependent travel times, Figure 4b) are then calculated relative to the synthetic model by cross correlating the isolation filter with the data and the full synthetic; the filter/data cross correlation provides the initial phase delay estimates, and the filter/synthetic cross correlation captures the interference expected from wavegroups not modeled by the filter, for which the final phase delays are corrected. In this case, the *SSS* waveform is moderately dispersed relative to the synthetic model, with low frequencies arriving approximately as predicted, and higher frequencies arriving up to 8 s early. Each phase delay has a corresponding partial derivative kernel (Figure 4c), which provides the sensitivity of the observation to perturbations in the model. Vertical-component *SSS* is sensitive to all 6 parameters of the anisotropic model, but we plot only v_{SH} and v_{SV} for clarity (cf. Figure 8). At low frequency, the *SSS* phase is sensitive primarily to the average SV velocity in the upper 500 km. At higher frequency, the kernel becomes more oscillatory, and while it still roughly averages over the upper 600 km, it is more sharply peaked near its ray-theoretical turning point at approximately 500 km depth.

Love waves from shallow-focus events provide excellent sensitivity to the SH velocity structure in the uppermost mantle, but they traditionally have been very difficult to study because they cannot be described simply in terms of ray paths or single mode branches [e.g. *James*, 1971]. The GSDF technique is especially useful for extracting phase delays and partial derivative kernels

for such complex phases. Figure 6a contains an observed tangential-component seismogram from a shallow focus earthquake; the direct *S* and Love waves are the only observed phases in this time window. Also shown are a complete synthetic seismogram and an isolation filter (labeled Filt1) that is calculated via summation of the fundamental mode branch. A comparison between Filt1 and the full synthetic indicates that the branch summation captures only a portion of the full Love waveform, and thus represents a case which requires the application of interference corrections to successfully extract phase delays and partial derivative kernels. The magnitude and importance of these corrections are clear from Figures 6b and 6c (with notation consistent with *Gee and Jordan*, [1992]). In Figure 6b, the symbols labeled $\delta\tau_p + \tilde{t}_p$ are the phase delays resulting directly from the cross-correlation of Filt1 with the data, where $\tilde{t}_p$ represents the correction terms determined from the cross-correlation of Filt1 with the full synthetic. The final phase delays ($\delta\tau_p$) that result from applying this correction term are up to 5 s slower that the initial estimates. Likewise, the partial derivative kernels (Figure 6c) corresponding to uncorrected $\delta\tau_p + \tilde{t}_p$ (labeled "Fund only", i.e. kernels containing only the contributions of the fundamental mode branch) are very different than the corrected kernels (labeled "complete"), which have a broader double peak that is more representative of the multimode nature of the full waveform. Clearly, if simple fundamental mode kernels are used to interpret the phase behavior of this waveform (as would be the case in typical surface-wave analyses), incorrect model perturbations would result.

Figure 7 illustrates the accuracy of the $\tilde{t}_p$ correction terms. Figure 7a contains the same data and full synthetic as in Figure 6, but now the isolation filter (labeled Filt2) is constructed by selecting all modes with group velocities of 4.14-4.54 km/s and phase velocity < 8 km/s (much like the "body wave" filter shown in Figure 5). Unlike Filt1, Filt2 clearly represents a good match to the full synthetic love wave, and the correction terms $\tilde{t}_p$ for this filter are negligible. The final $\delta\tau_p$ and partial derivative kernels for both filters are compared in Figures 7b and 7c, respectively, and they are nearly identical. The corrections applied to the phase delays and partial derivative kernels corresponding to the Filt1 accurately account for interference with modes not incorporated in the filter itself. Similar results are found for filters constructed by summing either the 1st or 2nd

higher mode branches, which contribute significantly to the full Love waveform. The extracted phase delays and partial derivative kernels are invariant for a variety of reasonable choices of isolation filters, demonstrating the power and robustness of the GSDF approach for handling complex waveforms.

We generate isolation filters for all observed R_1, G_1, *S*, *SS*, and *SSS* waveforms with sufficiently high signal-to-noise ratio; a total of 233 waveforms from the 55 events. Over 1500 frequency-dependent phase delays are extracted from the 233 waveforms. As shown by representative partial derivative kernels for each of these phase types (Figures 5, 7, and 8), the combination of surface-wave, reflected-body-wave, and direct-body-wave data provides good sensitivity to shear velocity structure throughout the upper 1000 km of the mantle. While the Rayleigh wave kernel (Figure 8a) is confined to the upper 300 km of the mantle, the *SSS* and *SS* kernels (Figures 5c and 8b) sample the upper 600 km, increasing our resolution of anisotropic structure in the sublithospheric mantle beyond that provided by surface waves alone. The frequency-dependent variability of these kernels demonstrates the advantage of our broad-band analysis of these "body" waves relative to a more typical narrow-band analysis at a single center frequency. The path-average, finite-frequency *S* wave (Figure 8c) also averages over much of the upper mantle and transition zone, with a peak near its ray-theoretical turning point at ~1000 km. As can be seen from Figure 8, the sensitivity of the observations to density, P and η structure is not negligible (with the exception of P and η kernels for tangential-component observations, which are zero), and we include these parameters in our inversion.

Figure 9 summarizes the GSDF data from all 55 events. These averages are for display only; our inversion includes the 1500 individual observations. All data have been corrected for source and receiver anomalies, which are calculated by averaging the tangential and vertical broad-band *S*-wave delays for each event. The large difference in the Love and Rayleigh wave residuals (5-25 s) relative to isotropic model PA2 is the *LR* discrepancy, and points to the presence of anisotropy in the upper mantle. In addition, the strong frequency-dependent trend in the Rayleigh-wave residuals indicates that PA2 does not correctly predict the Rayleigh-wave dispersion; the

trend of this relative dispersion favors a thinner lid and/or a slower LVZ. The Love wave phase delays reflect the interference between the fundamental and higher-mode Love waves (as shown above), and thus are not strongly dispersed relative to PA2, though they are much faster. Shear-wave splitting is observed in the *SS* and *SSS* phases, with the SSS_H and SS_H phases being advanced by up to 8 s and 4 s, respectively. This apparent splitting is frequency-dependent, with low-frequency observations be more split than high-frequency observations. The low-frequency *SSS* and *SS* observations are more sensitive to the shallow upper mantle than the high-frequency observations (see Figures 5 and 8), and thus this frequency-dependence places strong constraints on the depth extent of anisotropic structure. The *S* waves show little evidence of splitting or relative dispersion, indicating that the lower mantle is isotropic.

INVERSION

We invert our *ScS*-reverberation and turning-wave data set for perturbations to isotropic starting model PA2 using an iterative, linearized perturbation scheme in which the elastic parameters, density, and discontinuity depths are adjusted to minimize a chi-squared measure of misfit. Perturbations to depths to discontinuities and intercepts and slopes of the six radially anisotropic parameters within each of 7 upper mantle layers result in a total of 94 parameters. The data vector (1500 frequency-dependent travel time residuals, 8 vertical travel time residuals, and 7 discontinuity impedance contrast residuals) and perturbation matrix elements are described in the previous section. The observations are assumed to be independent, with *a priori* error estimates assigned based on the quality and resolution expected for the observation. For the GSDF data, error estimates range from 2 s for a high-quality, high-frequency (40 mHz) observation to 10 sec or larger for a fair quality, low-frequency (10 mHz) observation. We have estimated the errors of the ScS reverberation observations by considering the brightness of the reflector. The error estimates range from 0.005 for δR_o and 1.0 s for δt for the well-resolved 660 km and 410-km discontinuities, to 0.01 and 2.0 s for the more poorly resolved 520-km discontinuity. The model parameters are also assumed to be independent, with nominal prior error values of 10 km for

depths to discontinuities and 0.5 km/s for velocity values. These error values are quite generous and do not significantly damp the solution, with two exceptions. One is the slope in the transition zone, which needs to be slightly damped due to the flexibility allowed in the solution via the 520-km discontinuity. The second is in the P velocities in the upper 200 km, as discussed below.

The best-resolved parameters are the depths to discontinuities, the vertical shear impedance contrasts (i.e. a combination of v_{SV} and density), and the shear velocities, while the P velocities, η, and density are all relatively poorly determined by our data. We therefore constrain the solution to satisfy prior distributions on functions of the model parameters [e.g. *Tarantola*, 1987], based on mineral physics data for a pyrolite mantle composition. In particular, the density and bulk sound velocity (v_ϕ, where $v_\phi^2 = v_P^2 - \frac{4}{3}v_S^2$) can be reliably calculated for hypothesized mantle compositions [*Ita and Stixrude*, 1993], and we utilize these parameters to ensure that our P-velocity and density models are consistent with our well-constrained S-wave models (Figure 10). The constraint equations are summarized as follows:

1) Density. Between 200 and 660 km depth, density is required to roughly match the density calculated for pyrolite [*Ita and Stixrude*, 1993]. Below the 660 km discontinuity, this constraint is adjusted slightly to allow the density to more closely match the value typically inferred for the lower mantle [i.e. PREM, *Dziewonski and Anderson*, 1981], which is slightly higher than pyrolitic. The model is constrained to approximate the PREM value above 200 km depth. In general, the pyrolite density profile is nearly identical to PREM throughout the upper mantle, so choice of this particular profile is not important. The most important effect of constraining the density is the requirement that it be relatively smooth across the G, L, and 520-km discontinuities. In the case of G, this forces v_{SV} to account for most of the observed impedance contrasts; as shown below, this is generally consistent with the surface wave data as well. No impedance contrast is observed at L, so the requirement that density is 1st-order continuous is trivial. Near 520-km, a discontinuity is observed in the *ScS* reverberations but is not found in the density profiles. Forcing the entire observed impedance contrast into the v_{SV} structure produces a large, sharp 520 discontinuity, which has not been observed in other regions [*Jones et al.*, 1992];

alternatively, slightly relaxing the density constraint allows a minor density jump across this boundary that is consistent with both seismic results and some alternative mineral physics observations [*Rigden et al.*, 1991]. This jump is still within the error we assume for the constraint profiles.

2) Bulk sound velocity. Below 200 km depth, the P velocities are required to complement the S velocities such that the bulk sound velocity matches that calculated for a pyrolitic upper mantle [*Ita and Stixrude*, 1993]. Above 200 km, the P velocities are moderately well-constrained by the Rayleigh wave observations, so we simply damp the solution using slightly smaller prior constraints on the model to maintain reasonable values. Like the density, the bulk sound velocity across the G, L, and 520-km discontinuities is required to be first-order continuous, as the expected bulk modulus and density jumps across these horizons are expected to be minor [*Revenaugh and Jordan*, 1991c; *Ita and Stixrude*, 1993]. This still allows the individual velocities to be quite discontinuous if the data require it. In this case, both G and 520 are discontinuous in v_S and v_P, but first-order continuous in v_ϕ.

3) η. The anisotropic parameter η is constrained to be 1.0 in all isotropic layers, and between 0.9 and 1.0 in all anisotropic layers. These values are similar to those in PREM, and transversely isotropic models with a vertical axis of symmetry inferred from data sampling olivine or pyrolite material with a horizontal axis of symmetry should result in $\eta<1$ [*Nataf et al.*, 1986; *Montagner and Anderson*, 1989]. Correctly inferring the behavior of η is not critical for evaluating the shear wave anisotropy, as v_{SV} trades off only slightly with this parameter, and v_{SH} is largely independent of it. However, both v_{PV} and v_{PH} strongly trade off with η, and these parameters will be incorrect if we do not have η approximately correct.

A unique aspect of our inversions is our ability to selectively constrain the model to be isotropic within particular layers. We enforce isotropy (i.e. $v_{SH}=v_{SV}$, $v_{PH}=v_{PV}$, $\eta=1$) using linear constraint equations, and invert for a number of models in which we vary the regions that are allowed to be anisotropic. By evaluating the comparing misfit of each resulting model, we can determine the necessity of anisotropic structure within each layer, as well as the trade-offs of

allowing anisotropy within particular combinations of layers. In general, we assume that the crust and the transition zone are isotropic, and concentrate on anisotropic structure in the upper mantle.

The linearized inversion must be iterated to assure convergence to a final model, with each iteration requiring complete reprocessing of the GSDF data using new synthetics, isolation filters, and partial derivative kernels for the improved model. The results presented here represent three complete iterations.

RESULTS

Model PA5

Our preferred model (termed PA5) for central Pacific corridor from Tonga/Fiji to Hawaii is presented in Figure 11 and Table 3. This model does not uniquely fit our data, but it provides the best fit to our data within the context of our *a priori* expectations, as discussed below. PA5 is characterized by a high velocity (v_{SH} = 4.84 km/s), thin, anisotropic lithosphere, bounded at 69 ± 4 km depth by a large, negative G discontinuity; high v_{SH} (4.56 km/s) at the top of the LVZ, with a strong negative gradient leading to a minimum velocity (4.34 km/s) at 166 ± 20 km depth; v_{SV} in the lid of 4.65 km/s; low v_{SV} at the top of the LVZ (4.37 km/s) with a slight negative gradient to a velocity of 4.26 km/s at 166 km depth; and an isotropic high-gradient region from 166 km depth to the 410-km discontinuity. The transition zone discontinuities are located at 415 ± 3 km, 507 ± 10 km, and 651 ± 4 km. The shear anisotropy is 3.8 ± 0.5% in the lithosphere, 4.1 ± 0.5% at the top of the LVZ, and grades to nearly zero at the base of the LVZ; the small discontinuity at the base of the anisotropic region is below the detection level of *ScS* reverberations. The accompanying P anisotropy is approximately 3% through the lid and LVZ. The gradient between 166 km and the 410 discontinuity is quite steep, and the velocities in this depth range and into the transition zone are nearly identical to those found in regional isotropic oceanic models ATL [*Grand and Helmberger*, 1984b] and PA2 [*Lerner-Lam and Jordan*, 1987], which are designed to fit long-period SH and PSV waveforms, respectively. The final density and bulk sound velocity profiles generally satisfy the bulk sound velocity constraints (Figure 10).

The fit to our data is summarized in Figure 9 and Table 1; over 90% of the variance observed relative to PA2 is explained by PA5. The SH-SV differences observed in the surface wave, *SSS* and *SS* phase delays have been eliminated, the relative dispersion is removed, and the *ScS*-reverberation data is now largely satisfied. Two apparent inconsistencies are found in the *ScS*-reverberation data. The impedance contrast across the Moho must be larger than the *ScS* data indicate in order to maintain reasonable crustal velocity and density values. Also, the travel time to and impedance contrast at the G discontinuity is difficult to fit without thinning the lid further and raising lithospheric v_{SH} above 4.9 km/s, higher than typically observed *Sn* velocities from the central Pacific. The largest reported *Sn* velocity is 4.88 ± 0.12 km/s, observed just east of the Izu trench in the western Pacific [*Shimamura et al.*, 1977], and the large majority of Pacific *Sn* observations consistently show velocities less than 4.8 km/s [e.g. *Walker*, 1977]. These observations place rough constraints on our models, although they are not strictly applied because the measured travel times of the emergent *Sn* phase within the *P* coda may be systematically biased towards slower times. The G discontinuity may be one of the more difficult discontinuities to extract reflectivity information from due to interference from other shallow upper-mantle reflectors such as M and H [*Revenaugh and Jordan*, 1991c]; therefore, the 2 s t_v residual and 0.02 R_o residual relative to PA5 may be within realistic error estimates. An alternative model which fits the travel time to G has the same general anisotropic characteristics, and our conclusions do not change regarding these characteristics.

A simple (though qualitative) evaluation of PA5 can be made by visual comparison of data and synthetic waveforms. Figure 12 presents a suite of observed seismograms that characterize our data set, along with full mode-synthetic seismograms calculated for PA5. All phase types are represented, including *S*, *R1*, *G1*, and (for 870907) *SS* from shallow events, *S*, *SS*, and *sSS* from intermediate events, and *S*, *SS*, and *SSS* from deep events. While there is obvious variability and misfit in some cases, the overall fit to this complex suite of waveforms is quite good, especially considering the additional complexity added by unmodeled interfering phases such as *sS*, *ScS*, and *sScS*; in fact, observable misfit is almost always in a region of such

interference. Note that these events are truly representative of our data set in that they were chosen not because of the particularly good fit between data and synthetic, but rather because they represent a variety of source depths and distances with strong signal on both tangential and vertical components.

Depth Extent of Anisotropy: Alternative Models

Model PA5 contains anisotropic structure between M and 166 km depth, throughout the lid and LVZ. Can alternative distributions of anisotropy provide acceptable fits to the data within the context of our *a priori* expectations? Azimuthal variations in *Pn* velocity [*Shearer and Orcutt*, 1986] convincingly demonstrate that oceanic lithosphere is anisotropic, so we first explore the possibility that our data can be satisfied if the anisotropy is explicitly restricted to this region, with the LVZ and deeper regions strictly isotropic. This hypothesis is rejected because the SH velocity in the lid (>5.0 km/s) in such models is much greater than the highest observed *Sn* velocities, and because such models cannot explain the complex interference effects observed in the multi-mode Love waves across our distance interval. Figure 13 displays a transversely polarized seismogram (Δ=40.6°), with the direct *S* wave arriving at ~13.5 min and the emergent Love-wave group at ~16 min. The trace labeled PA3 is a complete synthetic seismogram for an earth model where anisotropy is restricted to the lithosphere [*Gaherty et al.*, 1992]. Synthetics of the first four mode branches for this model are displayed above the full synthetic (*topmost traces*), showing that the impulsive Love wave results from the constructive interference among the 0th, 1st, and 2nd mode branches. (Note that the first two overtones are larger in amplitude than the fundamental mode.) It is very difficult to dephase these branches to generate an emergent waveform by adjusting the lithospheric velocity; models with SH velocities less than ~4.4 km/s at the top of the LVZ generally produce impulsive waveforms of this type, regardless of lid velocity. In comparison, the trace labeled PA5 is a complete synthetic for our preferred model with anisotropy extending into the LVZ. The increased SH velocity in the LVZ enhances and advances the 0th and 1st mode branches (shown in *lowermost traces*), thereby generating a complete synthetic with emergent, dispersed behavior similar to that observed in the data. Waveforms such as these provide strong

evidence for the presence of relatively high SH velocities in the LVZ. The dispersive characteristics observed in the Rayleigh waves require low SV velocities in this depth range, and thus we are convinced that anisotropy extends into this region.

We also test the alternative hypothesis that anisotropy is preferred throughout the upper mantle to the 410-km discontinuity. The *S* and *SS* splitting data constrain the magnitude of the anisotropy within the high-gradient region below the LVZ to be small (<1%), and inversions that allowed anisotropy in this layer yielded no significant improvement in the fit to the data relative to PA5. The data are therefore consistent with the base of the LVZ roughly corresponding to the lower boundary of the anisotropic layer.

Azimuthal Anisotropy

The primary indicator of anisotropy in data collected along a single azimuth such as ours is the *LR* discrepancy and the associated phenomenon (SH-SV splitting) observed in the upper-mantle shear waves. Interpretation of the resulting radially anisotropic model in terms of the actual anisotropic structure of the mantle is indirect, as apparent radial anisotropy may arise from a number of phenomena, and some assumptions must be made in order to offer any interpretation. It is common to assume that upper-mantle anisotropy arises via crystallographic orientation of olivine and pyroxene, which can be aligned by the flow fields of plate tectonics [*Estey and Douglas*, 1986; *Nicolas and Christensen*, 1987; *Kern*, 1993]. Ophiolite samples [*Nicolas and Christensen*, 1987] and seismic refraction experiments [*Raitt et al,* 1969; *Shearer and Orcutt*, 1986] indicate that olivine crystals in oceanic lithosphere systematically align with a fast axis in the horizontal plane parallel to the direction of fossil spreading. Arguments have also been made that olivine crystals can align with fast axes parallel to current dynamic motion in the sublithospheric upper mantle [*Montagner and Tanimoto*, 1991; *Vinnik et al*, 1993; *Russo and Silver*, 1994; *Su and Park*, 1994], although this notion remains controversial due to the difficulty in isolating the deeper mantle signature. The magnitude of the *LR* discrepancy and SH-SV splitting is strongly dependent on the angle between the propagation azimuth and the fast-axis direction [*Maupin*, 1985], and therefore single-azimuth radially anisotropic models will also be dependent on this relative

propagation angle. If we assume that our observed anisotropy arises from such a structure, PA5 is consistent with olivine alignment throughout the lid and LVZ with a fast axis trend in the azimuth range of 225°-360°. This range encompasses both the direction of current plate motion and the fossil spreading direction along this path (Figure 1), and both mechanisms are consistent with our model.

Consider, however, the propagation path from the Kuril seismic zone to Hawaii (Figure 14), which samples oceanic lithosphere nearly identical (both in age and fossil spreading direction) to the Tonga-Hawaii path, yet provides nearly orthogonal sampling relative to the current plate motion direction. The simple fossil-spreading/current-plate-motion models predict that lithosphere-sensitive observations (in particular, surface waves with frequencies greater than ~ 30 mHz) should be similar between the two paths, but deeper-sampling observations (lower-frequency surface waves and multiply-reflected body waves) should have a greatly reduced (by several seconds) *LR* and SH-SV discrepancy on the Kuril path. Figure 14 presents the phase delays of surface and multiply-reflected body waves from the Kurils along with those from Tonga/Fiji. The nearly identical splitting in the R_1/G_1, *SS*, and *SSS* phases from both the Kuril and Tonga/Fiji events is strong evidence against coherent large-scale azimuthal anisotropy generated by current plate motion in the western Pacific. In fact, PA5 provides a remarkably good fit to the Kuril data, indicating that the (relatively) common lithosphere structure is the source of the observed anisotropy along the two paths.

DISCUSSION

Fossil vs. Dynamic Anisotropy and the Mechanical Structure of Oceanic Upper Mantle

One of our principle results is that seismic anisotropy beneath the central Pacific can be constrained above approximately 170 km depth. Taken at face value, the continuity of anisotropic structure across the inferred base of the lithosphere (the G discontinuity) indicates that both "fossil" (frozen in during ancient tectonic events) and "dynamic" (due to current mantle flow) forms of anisotropy are present in oceanic upper mantle, in agreement with results from long-

period surface-wave and higher-mode analyses from the central Pacific [*Regan and Anderson*, 1984; *Nataf et al.*, 1986; *Cara and Lévêque*, 1988; *Nishimura and Forsyth*, 1989; *Montagner and Tanimoto*, 1991]. The maximum depth extent of the anisotropy is somewhat shallower than inferred from these studies, however, perhaps in agreement with the results of *Ribe* [1989], whose numerical results indicate that crystallographic alignment leading to observable anisotropy will only occur in regions of progressive simple shear, in this case relatively close to the base of the plate. The lack of azimuthal variation in our data indicates that the dynamic anisotropy is due to a mechanism other than coherent large-scale current plate motion; small-scale convection beneath the plate [*Parsons and McKenzie*, 1978] represents one such mechanism.

It is possible, however, that G does not represent a major mechanical boundary. The sharp drop in velocity and an accompanying increase in seismic attenuation [*Sato et al.*, 1989; *Revenaugh and Jordan*, 1991c] probably implies a rapid drop in the solidus, perhaps by an increase in the partial pressure of water [*Ringwood*, 1975]. While such a process may also reduce the long-term strength (viscosity) of olivine rocks by up to a factor of 30 relative to dry conditions [*Mackwell et al.*, 1985; *Karato et al.*, 1986], this weakening may not be significant relative to the order 10^4 temperature-dependent viscosity variation [*Schubert et al.*, 1976] across the 120 km-thick thermal boundary layer [*Carlson and Johnson*, 1993]. These numbers suggest that while the short-term elastic behavior of the upper mantle (and G) is controlled by homologous temperature, the long-term strength of the upper mantle is controlled primarily by temperature, and the mechanical lithosphere (and accompanying fossil anisotropy) extends into the LVZ to depths of order 100-120 km. Dynamic anisotropy may still form below this lithosphere/asthenosphere boundary, but now this anisotropic zone is much thinner, of order 50 km. This model is consistent with the similarity in anisotropic signature observed for the Kuril and Tonga/Fiji paths, which implies a dominant lithospheric component.

Our data cannot distinguish between these two models. It is clear from PA5 that anisotropy extends to depths beyond any reasonable thermal or mechanical thickness of the lithosphere, and therefore some amount of both dynamic and fossil anisotropy is required. This result contrasts

with the inferred rapid termination of anisotropy within the Australian continental lithosphere [*Gaherty and Jordan*, 1995], where the anisotropy is interpreted to be entirely fossilized. A dynamic component of anisotropy is consistent the relatively high temperatures and strain-rates in the sub-oceanic upper mantle. The relatively smooth termination of this dynamic component of anisotropy implies a significant gradient with depth in horizontal strains between 100-170 km depth.

Transition Zone Structure

The combination of *ScS*-reverberation data with *SS* and *SSS* travel times makes PA5 an excellent average model for examining the transition zone structure beneath the central Pacific. *Revenaugh and Jordan* [1991b] demonstrate that the general thermal properties of the transition zone can be inferred from the vertical travel times extracted from *ScS* reverberations, yet such inferences are dependent on mapping the travel times into a depth estimate through an assumed velocity model. The *SS* and *SSS* data allow us to fix the location of the discontinuities in velocity and depth, allowing a more concrete analysis of variability in depth and strength of the reflectors. In addition, we now have good estimates of the gradients between the discontinuities, which are particularly important for evaluating the mineralogy of the transition region [*Bass and Anderson*, 1984; *Duffy and Anderson*, 1989; *Ita and Stixrude*, 1993].

The steep velocity gradient between ~200 km depth and the 410-km discontinuity appears to be a robust feature of oceanic upper mantle. The velocities in this range are nearly identical to those observed in the North Atlantic [ATL, *Grand and Helmberger*, 1984a] and the Northwest Pacific [PA2, *Lerner-Lam and Jordan*, 1987]; in contrast, the gradient in this region is much more shallow in typical continental models [*Grand and Helmberger*, 1984b; *Lerner-Lam and Jordan*, 1987; *Gaherty and Jordan*, 1995], owing to the thick thermal boundary layer (tectosphere) extending to these depths beneath continents [*Jordan*, 1988]. This ocean-continent difference in our anisotropic models refutes the contention [*Anderson*, 1979; *Regan and Anderson*, 1984] that such features are the result of incorrect isotropic inversions. The bulk sound velocity calculated in PA5 is consistent with that calculated for either pyrolite or high-aluminum piclogite (Figure 10).

The location of the "410" is at 415 ± 3 km depth. This is somewhat deeper than that in either ATL or PA2, but it is nearly identical to the average value (414 ± 2 km) reported for the southwest Pacific and Australasia by *Revenaugh and Jordan* [1991b]. This indicates "average" mantle temperature at this depth, although the S and P velocities are slightly high relative to PREM, indicating temperatures slightly lower than average. The magnitude of this discontinuity is 4% in shear velocity, only slightly lower than *Revenaugh and Jordan's* average, and very similar to other regional and global models. The gradient below the 410-km discontinuity is again in excellent agreement with ATL, though it is somewhat shallower than PREM.

PA5 includes a 520-km discontinuity located at 507 ± 10 km, with an impedance contrast of 1.3% that is split into a 1.5% S-velocity increase and a 0.7% density increase. The presence of a global 520-km discontinuity has been advocated by *Shearer* [1990] and *Revenaugh and Jordan* [1991b], although its signature is at best minimal in short-period profiles [*Jones et al.*, 1992], and *Shearer's* [1990] results have been recently challenged [*Bock*, 1994]. Our *S*, *SS*, and *SSS* data provide good constraints on the average velocity structure of the transition zone, but they offer little help in characterizing a 520-km discontinuity due to their relatively long wavelengths. The presence of a 520 in the reflectivity profile (Figure 2) leads us to include it in our model. In addition, the density and bulk sound velocity profiles for pyrolite and piclogite both have "breaks" in slope at this point [*Ita and Stixrude*, 1993] (due to the β-phase to γ-spinel transition), and *Rigden et al.* [1991] argue that a significant density jump combines with a small velocity jump at this phase boundary to produce a shear impedance contrast of up to 5%. Given the uncertainties in the mineral physics observations and the limited bandwidth and/or geographic distribution in the seismological observations, we maintain a discontinuity that conservatively fits our *ScS*-reverberation observation with a discontinuity in both velocity and density.

The gradient between 507 km and the 660-km discontinuity are shallow relative to ATL and PA2, primarily because of the 520-km discontinuity. The average velocity in this depth range is about the same for the three models. PREM incorporates a very flat gradient just above the 660-km discontinuity that has a similar gradient to PA5. The low-velocities just above the discontinuity

and the relatively shallow depth (651 ± 4 km) indicate relatively high temperatures at this depth in this region.

Comparison with 3-D model S12_WM13

We stated in the introduction that our regional path-average models representing well-chosen corridors could better characterize some aspects of upper-mantle variability between tectonic environments than global three-dimensional parameterizations. As evidence supporting this claim, we contrast the lid and LVZ structure in PA5 and a 1-D path-average projection of the global 3-D model S12_WM13 [*Su et al.*, 1994] along the Tonga-Hawaii path ("S12TH"; Figure 15). The differences are dramatic: PA5 is over 4% faster than S12TH throughout the lid, while S12TH is much faster below the 220 km discontinuity. S12TH also maintains a flat gradient from 220-km to 400-km depth. Low lid velocities and a 220-km discontinuity with high velocities just below it are characteristic of PREM (the starting model for the S12_WM13 inversion), and they remain in S12_WM13, probably because of that model's reliance on long-period surface waves to constrain upper-mantle structure. Such data essentially average the upper 300 km of the mantle (Figure 16a), and therefore they cannot distinguish between two dramatically disparate models such as PA5 and S12_WM13. The higher-frequency data incorporated in our study can easily distinguish between these two models (Figure 16b), and PA5 is clearly preferable. We note that S12_WM13 is constructed to fit data with frequencies less than 30 mHz, and therefore should not necessarily be expected to match data above this frequency. Extremely strong gradients in radial velocity structure are clearly required by such data, however, and such features apparently are not be resolvable with the lower-frequency data sets currently incorporated in 3-D parameterizations. This problem may be compounded by the extremely large perturbations necessary to move from PREM to a PA5-like structure in a linearized inversion. Use of a regionalized starting model reflecting oceanic structure for 3-D inversions may allow for first-iteration models that provide a better fit to higher frequency (10-50 mHz) data traversing oceanic regions. Until such models are available, we present PA5 as an average central Pacific upper mantle model, and we encourage those debating details of other oceanic features (e.g. the depth extent of ridges) to utilize regional

models that incorporate higher frequency data (such as *Nishimura and Forsyth* [1989], whose "Region 4" model provides a reasonable fit to a subset of our data) rather than relying solely on 3-D tomographic models that may omit important features of oceanic upper mantle.

CONCLUSIONS

We measure and analyze 1500 frequency-dependent travel times from three-component recordings of *R1*, *G1*, *SSS*, *SS*, and *S* waveforms and invert them in conduction with *ScS*-reverberation data for a one-dimensional, path-average, radially anisotropic model for Pacific upper mantle between Tonga-Fiji and Hawaii. The *ScS*-reverberation data allow us to invert for well-constrained depths and impedance contrasts of discontinuities, and the three-component frequency dependent travel times constrain the anisotropic shear velocity structure within this discontinuous framework. Mineral physics data place constraints on density and bulk sound velocity. We perform a number of inversions to test hypotheses on the depth distribution of the anisotropic structure, and we find that anisotropy must be present through the oceanic lithosphere and into the low-velocity zone to ~170 km depth. A small amount of anisotropy is allowable, but not preferred, below this depth. Other features of preferred model PA5 include a thin, high velocity seismic lithosphere bounded at ~70 km depth by a sharp G discontinuity, a well-defined low-velocity zone extending to ~170 km depth, no L (~200 km) discontinuity, and very high gradients in velocity between 170-415 km depth. PA5 provides a good fit to data traversing the Pacific from the Kuril seismic zone to Hawaii, indicating that anisotropy due to current plate motion in the western Pacific is negligible. We conclude from these results that the source of anisotropic structure in the western Pacific is an ancient tectonic signature frozen into the thermal lithosphere during ancient events (plate formation and thickening), although a small component of anisotropy due to small-scale dynamic motion in the asthenosphere seems likely.

Acknowledgments. Most of the figures were generated using the free software GMT [*Wessel and Smith,* 1991]. We thank the Harvard seismology group for regularly supplying the CMT

solutions, and for maintaining the Seismic Archive Facility, from which most of this data was collected. Data was also collected from the IRIS Data Management Center.

REFERENCES

Anderson, D.L., The deep structure of continents, *J. Geophys. Res., 84,* 7555-7560, 1979.

Anderson, D.L. and A.M. Dziewonski, Upper mantle anisotropy: evidence from free oscillations, *Geophys. J. R. astr. Soc., 69,* 383-404, 1982.

Bass, J.D. and D.L. Anderson, Composition of the upper mantle: Geophysical tests of two petrological models, *Geophys. Res. Lett., 11,* 237-240, 1985

Cara, M. and J.J. Lévêque, Anisotropy of the asthenosphere: the higher mode data of the Pacific revisited, *Geophys. Res. Lett., 15,* 205-208, 1988.

Carlson, R.L. and H.P. Johnson, On modeling the thermal evolution of the oceanic upper mantle: An assessment of the cooling plate model, *J. Geophys. Res, 99,* 3201-3214, 1994.

Dziewonski, A.M. and D.L. Anderson, Preliminary reference Earth model, *Phys. Earth Planet. Inter., 25,* 297-356, 1981.

Duffy, T.S. and D.L. Anderson, Seismic velocities in mantle minerals and the mineralogy of the upper mantle, *J. Geophys. Res., 94,* 1895-1912, 1989.

Estey, L.H. and B.J. Douglas, Upper mantle anisotropy: a preliminary model, *J. Geophys. Res., 91,* 11,393-11,406, 1986.

Forsyth, D.W., The early structural evolution and anisotropy of the oceanic upper mantle, *Geophys. J. R. astr. Soc., 43,* 103-162, 1975.

Gaherty, J.B., T.H. Jordan, and L.S. Gee, Relating upper-mantle discontinuities and anisotropy: inversion of phase-delay and *ScS*-reverberation data (abstract), *Eos Trans. Amer. Geophys. Union,* **73,** No. 43 supplement, 523, 1992.

Gaherty, J.B. and T.H. Jordan, Lehmann Discontinuity as the base of an anisotropic layer beneath continents, *Science,* submitted, 1995.

Gao, S., P.M. Davis, H. Liu, P.D. Slack, Y.A. Zorin, V.V. Mordvinova, V.M. Kozhevnikov, and R.P. Meyer, Seismic anisotropy and mantle flow beneath the Baikal rift zone, *Nature, 371,* 149-151, 1994.

Gee, L.S. and T.H. Jordan, Polarization anisotropy and fine-scale structure of the Eurasian upper mantle, *Geophys. Res. Lett., 15,* 824-827, 1988.

Gee, L. S., and T. H. Jordan, Generalized seismological data functionals, *Geophys. J. Int., 111,* 363-390, 1992.

Grand, S.P. and D.V. Helmberger, Upper mantle shear structure of North America, *Geophys. J. R. astr. Soc., 76*, 399-438, 1984.

Grand, S.P. and D.V. Helmberger, Upper mantle shear structure beneath the northwest Atlantic Ocean, *J.Geophys. Res., 89,* 11,465-11,475, 1984.

Gripp, A.E. and R.G. Gordan, Current plate velocities relative to the hotspots incorporating the NUVEL-1 global plate motion model, *Geophys. Res. Lett, 17,* 1109-1112, 1990.

Hess, H., Seismic anisotropy of the uppermost mantle under oceans, *Nature, 203,* 629, 1964.

Ita, J. and L. Stixrude, Petrology, elasticity, and composition of the mantle transition zone, *J. Geophys. Res.*, **97**, 6849-6866, 1992.

James, D.E., Anomalous Love wave phase velocities, *J. Geophys. Res., 76,* 2077-2083, 1971.

Jones, L.E., J. Mori, and D.V. Helmberger, Short-period constraints on the proposed transition zone discontinuity, *J. Geophys. Res., 97,* 8765-8774, 1992.

Karato, S.-I, S.S. Paterson, and J.D. Fitz Gerald, Rheology of synthetic olivine aggregates: Influence of grain size and water, *J. Geophys. Res, 91*, 8151-8176, 1986.

Kern, H., P- and S-wave anisotropy and shear-wave splitting at pressure and temperature in possible mantle rocks and their relationship to the rock fabric, *Phys. Earth Planet. Inter., 87*, 245-256, 1993.

Lerner-Lam, A.L. and T.H. Jordan, How thick are the continents?, *J. Geophys. Res., 92,* 14007-14026, 1987.

Ludwig, W.J. and R.E. Houtz, Isopach map of sediments in the Pacific ocean basin and marginal sea basins, Amer. Assoc. Petrol. Geol., Tulsa, Okla., 1979.

Mackwell, S.J., D.L. Kohlstedt, and M.S. Paterson, The role of water in the deformation of olivine single crystals, *J. Geophys. Res., 90,* 11,319-11,333, 1985.

Maupin, V., Partial derivatives of surface-wave phase velocities for flat anisotropic models, *Geophys. J. R. astr. Soc., 83,* 379-398, 1985.

McNutt, M.K. and A.V. Judge, The superswell and mantle dynamics beneath the South Pacific, *Science, 248*, 969-975, 1990.

Montagner, J.-P. and D.L. Anderson, Petrological constraints on seismic anisotropy, *Phys. Earth Planet. Inter., 54,* 82-105, 1989.

Montagner, J.-P. and T. Tanimoto, Global upper-mantle tomography of seismic velocities and anisotropy, *J. Geophys. Res., 96,* 20,337-20,351, 1991.

Mueller, R.D., Roest, W.R., Royer, J.-Y., Gahagan, L.M., and Sclater, J.G., A digital age map of the ocean floor, *SIO Reference Series 93-30*, 1993.

Nataf, H.-C., I. Nakanishi, and D.L. Anderson, Measurements of mantle-wave velocities and inversino for lateral heterogeneities and anisotropy, 3. Inversion, *J. Geophys. Res., 91,* 7261-7307, 1986.

Nicolas, A. and N.I. Christensen, Formation of anisotropy in upper mantle peridotites: A review, in *Composition, Structure, and Dynamics of Lithosphere-Asthenosphere Systerm, Geodyn. Ser.*, vol. 16, edited by K. Fuchs and C. Froidevaux, pp. 111-123, AGU, Washington, D.C., 1987.

Nishimura, C.E. and D.W. Forsyth, The anisotropic structure of the upper mantle in the Pacific, *Geophys. J., 96,* 203-229, 1989.

Parsons, B. and D. McKenzie, Mantle convection and the thermal structure of the plates, *J. Geophys. Res., 83,* 4485-4496, 1978.

Raitt, R.W., G.G. Shor, T.J. Francis, and G.B. Morris, Anisotropy of the Pacific upper mantle, *J. Geophys. Res., 74,* 3095-3109, 1969.

Regan, J. and D.L. Anderson, Anisotropic models of the upper mantle, *Phys. Earth Planet. Int., 35,* 227-263, 1984.

Revenaugh, J. S., and T. H. Jordan, Observations of first-order mantle reverberations, *Bull. Seis Soc. Am., 77,* 1704-1717, 1987.

Revenaugh, J. S., and T. H. Jordan, A study of mantle layering beneath the western Pacific, *J. Geophys. Res., 94,* 5787-5813, 1989.

Revenaugh, J.R. and T.H. Jordan, Mantle layering from *ScS* reverberations, 1, waveform inversion of zeroth-order reverberations, *J. Geophys. Res., 96,* 19,749-19,762, 1991a.

Revenaugh, J.R. and T.H. Jordan, Mantle layering from *ScS* reverberations, 2, The transition zone, *J. Geophys. Res., 96,* 19,763-19,780, 1991b.

Revenaugh, J.R. and T.H. Jordan, Mantle layering from *ScS* reverberations, 3, The upper mantle, *J. Geophys. Res., 96,* 19,781-19,810, 1991c.

Ribe, N.M., Seismic anisotropy and mantle flow, *J. Geophys. Res., 94,* 4213-4223, 1989.

Rigden, S.M., G.D. Gwanmesia, J.D. Fitzgerald, I. Jackson, and R.C. Lieberman, Spinel elasticity and the seismic structure of the transition zone of the mantle, *Nature, 345,* 143-145, 1991.

Russo, R.M. and P.G. Silver, Trench-parallel flow beneath the Nazca plate from seismic anisotropy, *Science, 263,* 1105-1111, 1994.

Ringwood, A.E., *Composition and Petrology of the Earth's Mantle,* 604 pp., McGraw-Hill, New York, 1975.

Sato, H., I.S. Sacks, T. Murase, G. Muncill, and H. Fukuyama, *Qp*-melting temperature relation in peridotite at high pressure and temperature: attenuation mechanism and implications for the mechanical properties of the upper mantle, *J. Geophys. Res, 94,* 10,647-10,661, 1989.

Schubert, G., C. Froidevaux, and D.A. Yuen, Oceanic lithosphere and asthenosphere: Thermal and mechanical structure, *J. Geophys. Res., 81,* 3525-3540, 1976.

Shearer, P.M., Seismic imaging of upper mantle structure with new evidence for a 520-km discontinuity, *Nature, 344,* 121-126, 1990.

Shearer, P.M. and J.A. Orcutt, Compressional and shear wave anisotropy in the oceanic lithosphere -- the Ngendei seismic refraction experiment, *Geophys. J. R. Astr. Soc, 87,* 967-1003, 1986.

Shearer, P.M. and T.G. Masters, Global mapping of topography on the 660-km discontinuity, *Nature, 355,* 791-796, 1992.

Shimamura, H., T. Asada, and M. Kumazawa, High shear velocity layer in the upper mantle of the Western Pacific, *Nature, 269,* 680-681, 1977.

Silver, P.G. and W.W. Chan, Shear wave splitting and subcontinental mantle deformation, *J. Geophys. Res., 96,* 16,429-16,454, 1991.

Sipkin, S. A., and T. H. Jordan, Lateral heterogeneity of the upper mantle determined from the travel times of multiple *ScS*, *J. Geophys. Res., 81,* 6307-6320, 1976.

Sipkin, S. A., and T. H. Jordan, Multiple *ScS* travel times in the western Pacific: Implications for mantle heterogeneity, *J. Geophys. Res., 85,* 853-861, 1980.

Su, W.-J., R.L. Woodward, and A.M. Dziewonski, Degree 12 model of shear velocity heterogeneity in the mantle, *J. Geophys. Res., 99,* 6945-6980, 1994.

Su, L. and J. Park, Anisotropy and the splitting of PS waves, *Phys. Earth. Planet. Inter., 87,* 1994.

Tarantola, A., *Inverse Problem Theory*, 613 p., Elsevier, New York, 1987.

Vidale, J.E. and H.M. Benz, Upper-mantle seismic discontinuities and the thermal structure of subduction zones, *Nature, 356,* 678-683, 1992.

Vinnik, L.P., L.I. Makeyeva, A. Milev, and A.Y. Usenko, Global patterns of azimuthal anisotropy and deformations in the continental mantle, *Geophys. J. Int., 111,* 433-447, 1992.

Walker, D.A., High-frequency *Pn* and *Sn* phases recorded in the western Pacific, *J. Geophys. Res., 82,* 3350-3360, 1977.

Wessel, P. and W.H.F. Smith, Free software helps map and display data, *EOS Trans. Amer. Geophys. U., 72,* pp. 441, 445-446, 1991.

Woodhouse, J.H. and A.M. Dziewonski, Mapping the upper mantle: Three-dimensional modeling of earth structure by inversino of seismic waveforms, *J. Geophys. Res., 89,* 5953-5986, 1984.

Zhang, Y.-S. and T. Tanimoto, High-resolution global upper mantle structure and plate tectonics, *J. Geophys. Res., 98,* 9793-9823, 1993.

FIGURE CAPTIONS

Fig. 1. Mercator projection of the Tonga/Fiji-to-Hawaii corridor sampled by our data. The propagation path (dotted line) is highly oblique to the fossil spreading direction (as depicted by plate age contoured in 25 Ma intervals) [*Mueller et al.*, 1993]) and is roughly perpendicular to current plate motion relative to a hotspot reference frame (arrow) [*Gripp and Gordan*, 1990]. Epicenters of the 55 Tonga-Fiji earthquakes are shown. Also shown are Aleutian and Kuril events used to test for azimuthal variations.

Fig. 2. (Left) Observed reflectivity profile and its interpretation obtained for central Pacific corridor, connecting events in the Tonga/Fiji seismic zone with station KIP. The profile and its interpretation both display normal-incidence SH reflectivity (R_o), in percent. Apparent depths in interpretation were computed using the aspherical M84C velocity structure of *Woodhouse and Dziewonski* [1984]; these depths are refined in the model presented in this paper. (Right) Seismic Q structure for the Tonga/Fiji to Oahu path. (a) Average Q_{ScS} from multiple-*ScS* observations. (b) Q_{UM} and Q_{LM} from *ScS*-reverberation observations. (c) A priori Q structure assumed for the modeling in this paper. Q_{UM} is partition into lid, LVZ, and transition zone values. The vertical average Q is maintained within each column, i.e. (c) maintains the average upper- and lower-mantle values in (b), and (b) maintains the average value in (a).

Fig. 3. Observational evidence of anisotropy in data from a shallow-focus (10 km depth) event. Top pair of traces are vertical-component data and full synthetic seismogram for isotropic model PA2, with an S wave arriving at ~14.5 min and a Rayleigh wave at ~20 min. The bottom pair of traces are tangential-component observation and synthetic seismogram for PA2, with the S wave again at ~14.5 min and multimode Love wave at ~18 min. Although the group arrival of the Rayleigh wave roughly matches the PA2 synthetic, the dispersion is quite different, and the fit to

the Love wave is extremely poor. Mode-summation synthetic seismograms are complete to 50 mHz, filtered like the data, and convolved with Harvard CMT source mechanism.

Fig. 4. Observational evidence for anisotropy in data from a deep focus (562 km depth) event. Top pair of traces are vertical-component data and full synthetic for PA2 centered on an *SSS* arrival at ~21 min. The bottom pair of traces are the tangential-component data and synthetic for this arrival. The synthetics have been shifted so that the vertical-component *SSS* synthetic is aligned with the data. The LPT *SSS* arrival is faster than PA2 (and the vertical-component *SSS* observation) by nearly half a cycle, over 10 s. SH-SV differences in phases such as this one place good constraints on anisotropy in the deeper upper mantle and the transition zone.

Fig. 5. Example of the GSDF processing, as discussed in the text. a) Observed (top), full synthetic (middle), and isolation filter (bottom) seismograms for vertical-component data from a deep focus event (472 km depth). Observed phases are *S* (13.5 min), *sS* (16 min), *SS* (17 min), and *sSS* (19 min). The isolation filter is for *sSS*, constructed by summing mantle modes with group velocities of 4.20±0.1 km/s. b) Phase delays $\delta\tau_p$ as a function of frequency, relative to the starting model. The frequency-dependent trend indicates the relative dispersion observed in these "body" waves, and illustrates the value of using a broad-band approach to processing the data. This data is fast at high frequencies, but is well fit by the model at low frequencies. c) Three sets of partial derivative kernels as a function of depth; the kernels relative to the two shear velocities for 15, 30, and 45 mHz are shown for this example. While the low-frequency observation (15 mHz) is sensitive to the SV structure of the upper 400 km, the higher-frequency observations become increasingly sensitive to structure in the transition zone.

Fig. 6. Example of the ability of GSDF to account for interference of complex waveforms. a) Observed (top), full synthetic (middle), and isolation filter (bottom) synthetics for tangential-component data from a shallow-focus (10 km depth) event. The *S* wave arrives at ~14.5 min, the

multimode Love wave at ~18 min. The isolation filter (Filt1) is constructed by summing only the fundamental mode branch, and thus it does not include higher mode contributions and is a poor match to even the full synthetic Love wave. b) Initial phase delay estimates $\delta\tau_p+\tilde{\imath}_p$, and final phase delays $\delta\tau_p$, as a function of frequency. The $\delta\tau_p$ have been corrected by up to 6 s by removing the interference term $\tilde{\imath}_p$. c) Partial derivative kernels for v_{SH} (solid line) that are used to invert the $\delta\tau_p$ observations in 6b. The dash line represents the kernels that would be used if the Love wave were assumed to be fundamental mode only (i.e. the interference corrections were not applied).

Fig. 7. a) Same data and full synthetic as Figure 6a, but with a new isolation filter (Filt2) constructed by summing all mantle modes with group velocities 4.34±0.2 km/s. This Filter represents an excellent match to the full synthetic Love wave, and interference corrections are negligible. b) Final phase delays $\delta\tau_p$ for both Filt2 and Filt1 from Fig. 6b.
c) v_{SH} partial derivative kernels for Filt2 and Filt1. The nearly identical behavior for the phase delays and kernels for these two filters demonstrates the robustness of the GSDF procedure.

Fig. 8. Partial derivative kernels for examples of different phase types. a) Rayleigh wave kernels. b) Tangential-component *SS* kernels. c) Vertical-component *S* kernels. For each phase, two frames are shown: low frequency (15 mHz) on the left, high frequency (40 mHz) on the right. Within each frame, 3 pairs of kernels are shown: shear kernels on the left, compressional kernels in the middle, and η and density kernels on the right. Relative scales are maintained for each phase, with a scale provide on the far right in units of s km^{-3} $unit^{-1}$ perturbation.

Fig. 9. Summary of the phase delay data. Phase delays are categorized by phase type (Surface wave, *SSS* , *SS*, or *S*), and then separated into tangential (SH) or radial/vertical (SV) observations, and averaged in each frequency band. Symbols represent the residuals relative to

PA2, while the lines represent the predicted fit of model PA5 to these data. Dispersion relative to PA2 is indicated by a frequency-dependent trend, while evidence of anisotropy can be observed as a separation of the SH and SV observations for a given phase type. a) Love and Rayleigh waves. b) *SSS* and *sSS* waves. c) *SS* waves. d) *S* waves. Error bars determined by a weighted average of estimated *a priori* errors.

Figure 10. Theoretical values of density ρ and bulk sound velocity v_ϕ calculated by *Ita and Stixrude* [1992] for the pyrolite model (*dashed lines*); *dotted lines* represent the ±2% error envelope for the calculated profiles. These were used to construct *a prior* distributions for ρ and v_ϕ that was used in the inversion. The values calculated from resulting model PA5 (*solid lines)* are shown for comparison. Neither the density nor the bulk sound velocity constraints are critically dependent on the choice of pyrolite for a model composition; the general behavior of both density and bulk sound velocity is similar for high-aluminum piclogite, for example.

Fig. 11. Model PA5. From left to right, η, density, shear velocities, and compressional velocities are plotted as a function of depth. The model is radially anisotropic through the lithosphere and the low-velocity zone, with v_{SH} and v_{PH} being higher than v_{SV} and v_{PV}, respectively. Below 800 km depth, the model is the same as PREM.

Fig. 12a. Comparisons between observed and synthetic seismograms from 4 representative shallow- and intermediate-focus events. Each event is represented by both tangential- (LPT) and vertical- (LPZ) component seismograms; for each event pair, the top trace is the data, the bottom trace is the seismogram (complete to 50 mHz) for final model PA5. The traces are aligned (at 0 min) on the *S* wave, with the synthetic seismograms further corrected for an event static. Both data and synthetic are low-passed with a 45 mHz corner.

Fig. 12b. Same as Figure 12a, except for 4 representative deep-focus events.

Fig. 13. Seismograms showing a multi-mode Love wave that is diagnostic of high v_{SH} in the LVZ. The observed seismogram (center trace, labeled *KIP*) is the transverse component recorded at KIP from a shallow-focus event. The direct *S* wave arrives at ~13.5 min and the emergent Love-wave group at ~16 min. The trace labeled PA3 is a complete synthetic seismogram for an earth model where anisotropy is restricted to the lithosphere. Synthetics of the first four mode branches for this model are displayed above the full synthetic (*topmost traces*, with the 0th mode branch being the thickest line, and the 3rd higher-mode branch being the thinnest). The trace labeled PA5 is a complete synthetic for PA5, where the anisotropy extends into the LVZ. The increased SH velocity in the LVZ enhances and advances the 0th and 1st mode branches (shown in *lowermost traces*), thereby generating a complete synthetic with emergent, dispersed behavior similar to that observed in the data.

Fig. 14. (*left*) Same map as Figure 1, but highlighting the additional western Pacific paths utilized to assess the azimuthal variability of upper mantle anisotropy in this region. In particular, note the significant difference in the angle between the Kuril-KIP path and the direction of current plate motion (nearly parallel), relative to the Tonga-KIP path (nearly perpendicular). Since the plate age is relatively constant between these two paths, this allows for a controlled experiment to evaluate the plate-motion signature of anisotropy. (*right*) Comparison of the *LR* discrepancy and SS_H - SS_V splitting between the three paths. Similarity of the splitting observations indicates that western Pacific upper mantle is largely radially anisotropic (and not azimuthally anisotropic) over these path lengths. In particular, similarity between the Kuril and Tonga/Fiji paths indicate that the current plate motion is not responsible for the bulk of the observed signal.

Fig. 15. Shear velocities for model PA5, a path-average approximation of S12_WM13 appropriate for the Tonga-Hawaii path (labeled "S12TH"), and PREM. For each model, the higher lid/LVZ velocity is v_{SH}, the lower velocity is v_{SV}. S12TH is calculated by determining the

average S12_WM13 perturbation to PREM as a function of depth over the path from Tonga/Fiji to Hawaii. Comparison between PA5 and S12TH indicates that S12_WM13 is too slow in the lithosphere and too fast near 220 km along this path, similar to (though less severe than) the discrepancy between PA5 and PREM.

Fig. 16. Observed and synthetic seismograms for models PA5 and S12_WM13, for a shallow-focus event. The *S* wave arrives at 14.5 min, the G_1 at ~18 min, and R_1 at ~20 min. Vertical component seismograms are on top, and tangential component seismograms are on the bottom. Synthetics are aligned on the *S* wave to remove the source static, and the S12_WM13 seismograms are calculated using the spherical harmonic coefficients and the asymptotic perturbation scheme of *Woodhouse and Dziewonski* [1984]. a) Seismograms low-pass filtered with a corner at 15 mHz. b) Seismograms low-pass filtered with a corner at 35 mHz.

Table 1. ScS Reverberation Data

Discontinuity	Observed		PA5 Prediction		PA2 Prediction	
	t_v	R_O	t_v	R_O	t_v	R_O
Moho	1.7	0.120	2.1	0.164	3.3	0.184
G	12.0	-0.055	14.2	-0.036	21.8	-0.034
L	----	0.000	36.8	0.004	41.1	0.008
"410"	91.1	0.046	91.8	0.039	89.7	0.045
"520"	107.7	0.021	109.7	0.013	----	0.000
"660"	136.6	0.078	136.5	0.080	141.2	0.071
CMB	470.1	----	468.5	----	470.1	----

t_v represents one-way travel time in seconds; R_O is the shear wave impedance contrast. Observations extracted from *Revenaugh and Jordan* [1991a,c].

Table 2. Tonga/Fiji Seismic Sources

Date	Harvard CMT Location				Station	Delta
	Origin Time UT	Latitude °N	Longitude °E	Depth km		°
1984 11 17	22:43:42.5	-18.28	-175.73	10	HON	43.01
1985 11 02	19:49:31.5	-18.21	175.99	10	HON	46.82
1988 04 02	14:26:39.8	-15.08	-172.96	15	HON	39.03
1989 04 08	03:06:08.7	-15.90	-172.91	15	HON	39.77
1991 01 01	17:28:08.4	-21.28	-173.98	15	KIP	45.21
1991 01 08	22:04:19.0	-17.76	-173.12	15	KIP	41.65
1991 02 09	02:08:57.0	-15.00	-176.81	15	KIP	40.62
1991 04 06	14:34:28.2	-14.86	-175.36	15	KIP	39.87
1991 04 19	11:25:37.3	-15.01	-174.90	15	KIP	39.81
1991 08 05	06:05:50.3	-21.58	-173.68	15	KIP	45.39
1983 09 17	12:11:43.1	-16.67	-177.24	16	HON	42.20
1987 01 09	08:01:40.2	-19.28	-176.52	17	HON	44.23
1983 05 15	00:24:01.4	-19.09	-175.72	20	HON	43.74
1990 09 08	20:32:06.5	-20.39	-173.96	21	KIP	44.38
1987 09 07	11:57:16.9	-28.06	-177.77	23	HON	55.55
1991 03 03	15:20:32.0	-22.09	-174.58	23	KIP	46.17
1988 12 05	16:05:44.7	-14.76	-173.49	44	HON	38.94
1985 06 03	12:06:29.7	-15.41	-173.28	46	HON	39.46
1991 10 30	10:35:51.9	-15.11	-173.07	48	KIP	39.19
1985 07 06	03:37:25.5	-29.50	-177.64	54	HON	53.95
1988 06 11	12:17:33.6	-15.06	-173.40	59	HON	39.18
1985 09 26	07:27:58.9	-34.79	-178.40	61	HON	59.07
1991 10 17	09:05:28.4	-14.83	-173.41	62	KIP	39.06
1987 11 03	08:15:09.5	-17.06	-173.55	107	HON	41.07
1988 01 29	16:48:11.7	-15.02	-173.71	119	HON	39.26
1988 02 06	21:30:11.0	-16.10	-173.49	124	HON	40.17
1989 01 02	01:52:14.5	-18.49	-174.39	128	HON	42.69
1984 04 18	06:49:21.9	-16.10	-174.02	158	HON	40.37
1988 07 19	01:00:24.9	-19.71	-174.39	159	HON	43.81
1991 11 11	16:15:55.2	-23.94	-176.97	179	KIP	48.71
1990 06 23	21:38:29.4	-21.29	-176.22	195	KIP	46.02
1986 10 30	01:29:05.1	-21.68	-176.45	196	HON	46.37
1987 03 19	22:51:45.9	-20.30	-175.96	215	HON	44.93
1988 01 15	08:40:30.5	-20.68	-175.77	221	HON	45.21
1986 06 28	05:03:55.4	-19.96	-175.71	222	HON	44.53
1984 06 15	14:22:32.8	-15.90	-174.66	270	HON	40.43
1991 06 09	07:45:10.9	-20.15	-175.90	292	KIP	44.86
1987 04 29	14:27:44.3	-19.06	-177.84	411	HON	44.58
1987 02 10	00:59:35.9	-19.47	-177.38	419	HON	44.75
1984 11 17	13:45:56.4	-18.84	-177.96	472	HON	44.43
1989 10 23	13:08:39.4	-25.51	179.15	480	HON	51.56
1990 06 08	15:05:19.2	-18.51	-178.93	504	KIP	44.66
1989 11 16	08:39:53.7	-17.36	-179.43	555	HON	43.80
1989 05 08	14:28:39.3	-23.62	-179.99	558	HON	49.53
1990 07 22	09:26:25.1	-23.15	-179.83	559	KIP	49.13
1983 06 20	05:43:41.8	-23.68	179.23	562	HON	49.92

Table 2. (continued)

Date	Harvard CMT Location				Station	Delta
	Origin Time UT	Latitude °N	Longitude °E	Depth km		°
1986 06 16	10:48:35.6	-21.86	-178.87	565	HON	47.50
1991 12 03	10:33:47.3	-26.11	178.69	575	KIP	52.37
1990 10 10	05:55:03.2	-23.08	178.93	575	KIP	49.61
1991 09 30	00:21:54.0	-20.67	-178.52	590	KIP	46.38
1990 07 11	19:48:17.0	-25.22	178.22	596	KIP	51.79
1989 04 16	19:48:22.9	-20.79	-179.18	601	HON	46.68
1986 05 26	18:40:54.5	-21.57	-179.30	603	HON	47.42
1990 06 26	12:08:38.5	-21.71	-179.60	614	KIP	47.76
1988 03 10	10:25:13.3	-21.02	-178.44	636	HON	46.57
1985 08 28	20:50:55.5	-20.89	-179.00	640	HON	46.70
1984 11 22	17:07:44.8	-17.72	-178.05	663	HON	43.48

Table 3. Model PA5

Depth, km	Density, gm/cm^3	v_{PV}, km/s	v_{SV}, km/s	v_{PH}, km/s	v_{SH}, km/s	η
0.0	1.030	1.500	0.000	1.500	0.000	1.00
5.0	1.030	1.500	0.000	1.500	0.000	1.00
5.0	1.500	2.010	0.920	2.010	0.920	1.00
5.2	1.500	2.010	0.920	2.010	0.920	1.00
5.2	3.027	5.933	3.684	5.933	3.684	1.00
12.0	3.027	5.930	3.685	5.930	3.685	1.00
12.0	3.339	8.036	4.654	8.274	4.836	0.90
69.0	3.379	8.058	4.665	8.296	4.832	0.90
69.0	3.350	7.877	4.372	8.051	4.560	0.90
166.0	3.410	8.043	4.257	8.086	4.335	1.00
166.0	3.417	8.063	4.286	8.063	4.286	1.00
415.0	3.578	8.924	4.840	8.924	4.840	1.00
415.0	3.713	9.286	5.038	9.286	5.038	1.00
507.0	3.849	9.640	5.195	9.640	5.195	1.00
507.0	3.879	9.708	5.283	9.708	5.283	1.00
651.0	4.024	10.108	5.431	10.108	5.431	1.00
651.0	4.292	10.757	5.972	10.757	5.972	1.00
791.0	4.457	11.078	6.231	11.078	6.231	1.00
791.0	4.457	11.078	6.231	11.078	6.231	1.00
801.0	4.462	11.104	6.240	11.104	6.240	1.00

Model is identical to PREM through the remainder of the lower mantle and core.

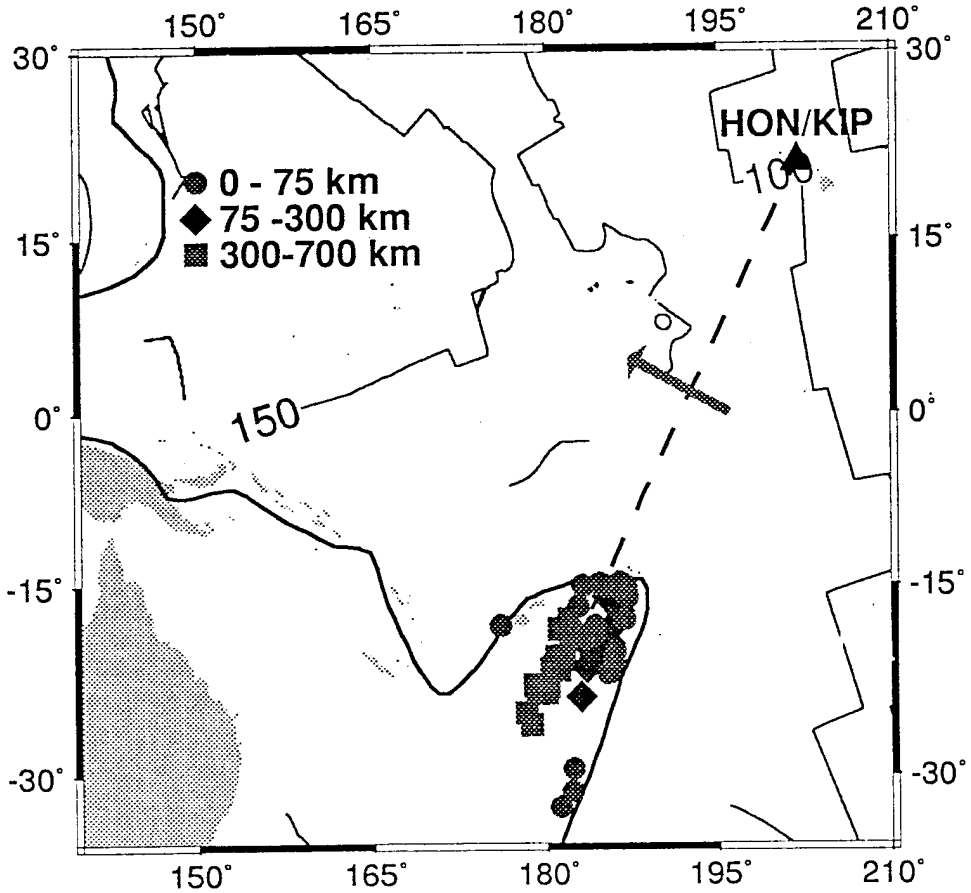
150°
165°
180°
195°
210°
30°
15°
0°
-15°
-30°
0 - 75 km
75 -300 km
300-700 km
HON/KIP
100
150

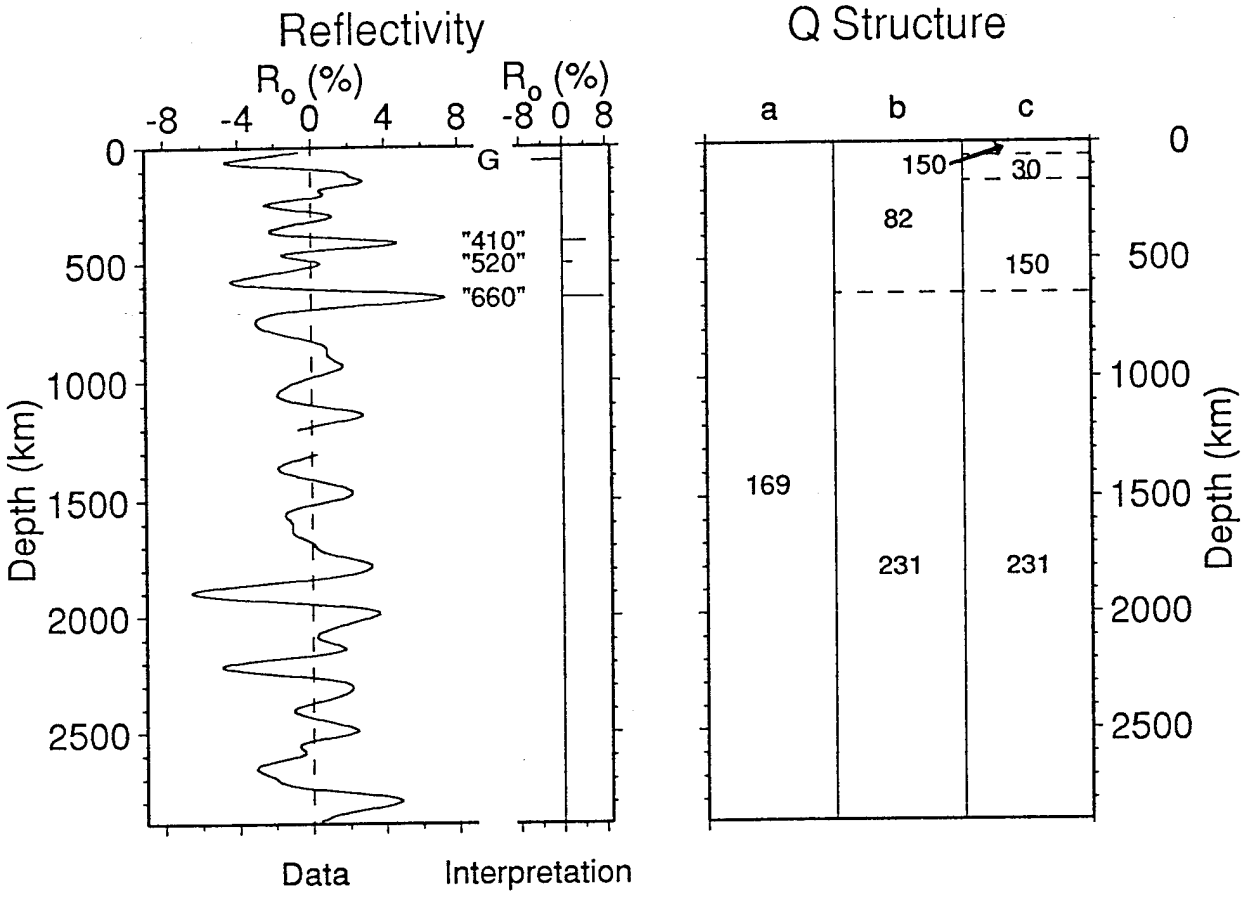
Reflectivity
Q Structure
R_o (%)
R_o (%)
-8 -4 0 4 8
-8 0 8
0
500
1000
1500
2000
2500
Depth (km)
G
"410"
"520"
"660"
Data
Interpretation
a
b
c
150
30
82
150
169
231
231
0
500
1000
1500
2000
2500
Depth (km)

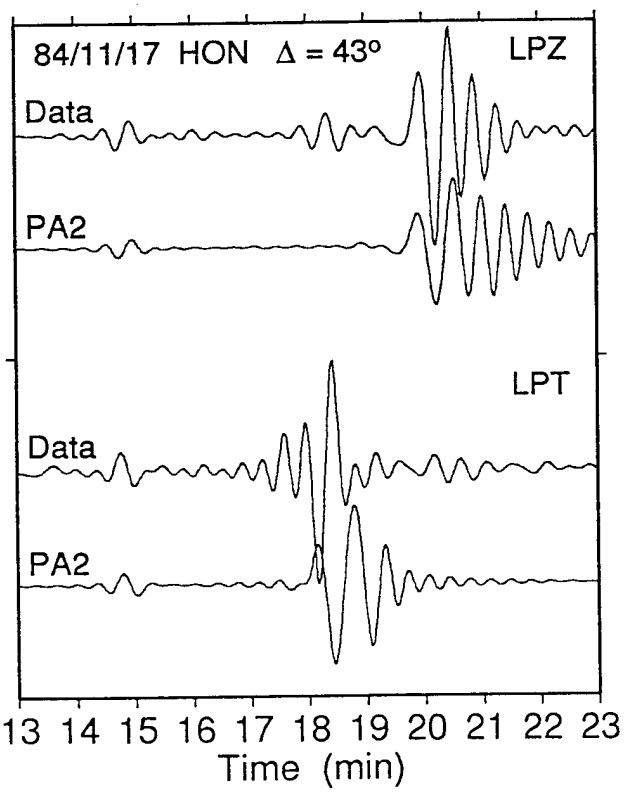
84/11/17 HON Δ = 43°
LPZ
Data
PA2
LPT
Data
PA2
13 14 15 16 17 18 19 20 21 22 23
Time (min)

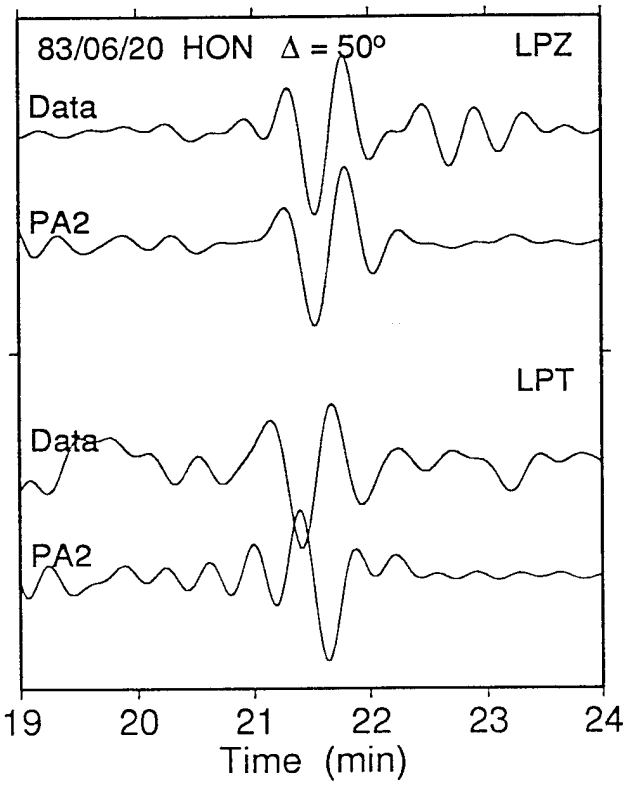
83/06/20 HON Δ = 50°
LPZ
Data
PA2
LPT
Data
PA2
19
20
21
22
23
24
Time (min)

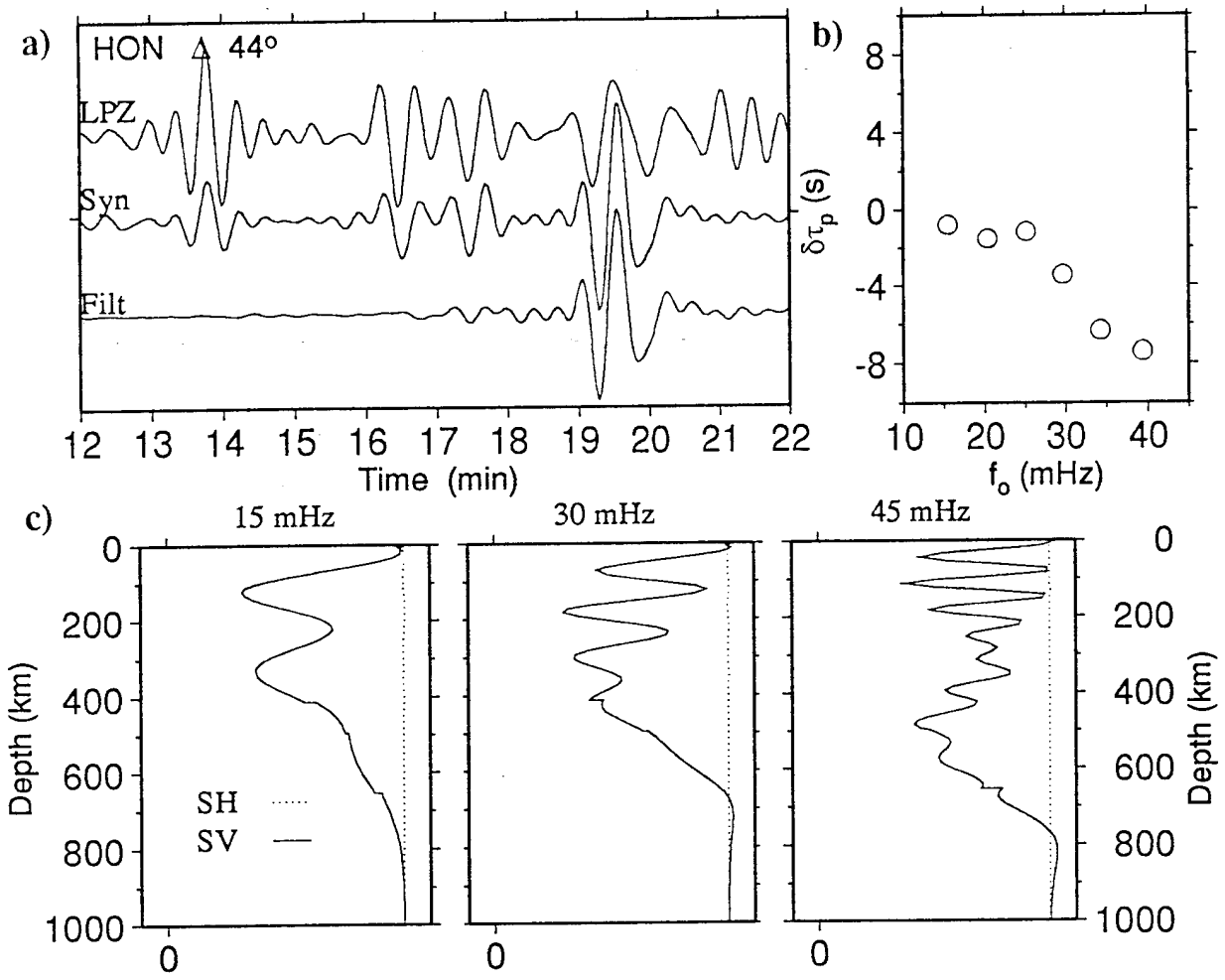

GMT Mar 10 14:22 pa3.ts 84111713 HON Z 4.20.02.8

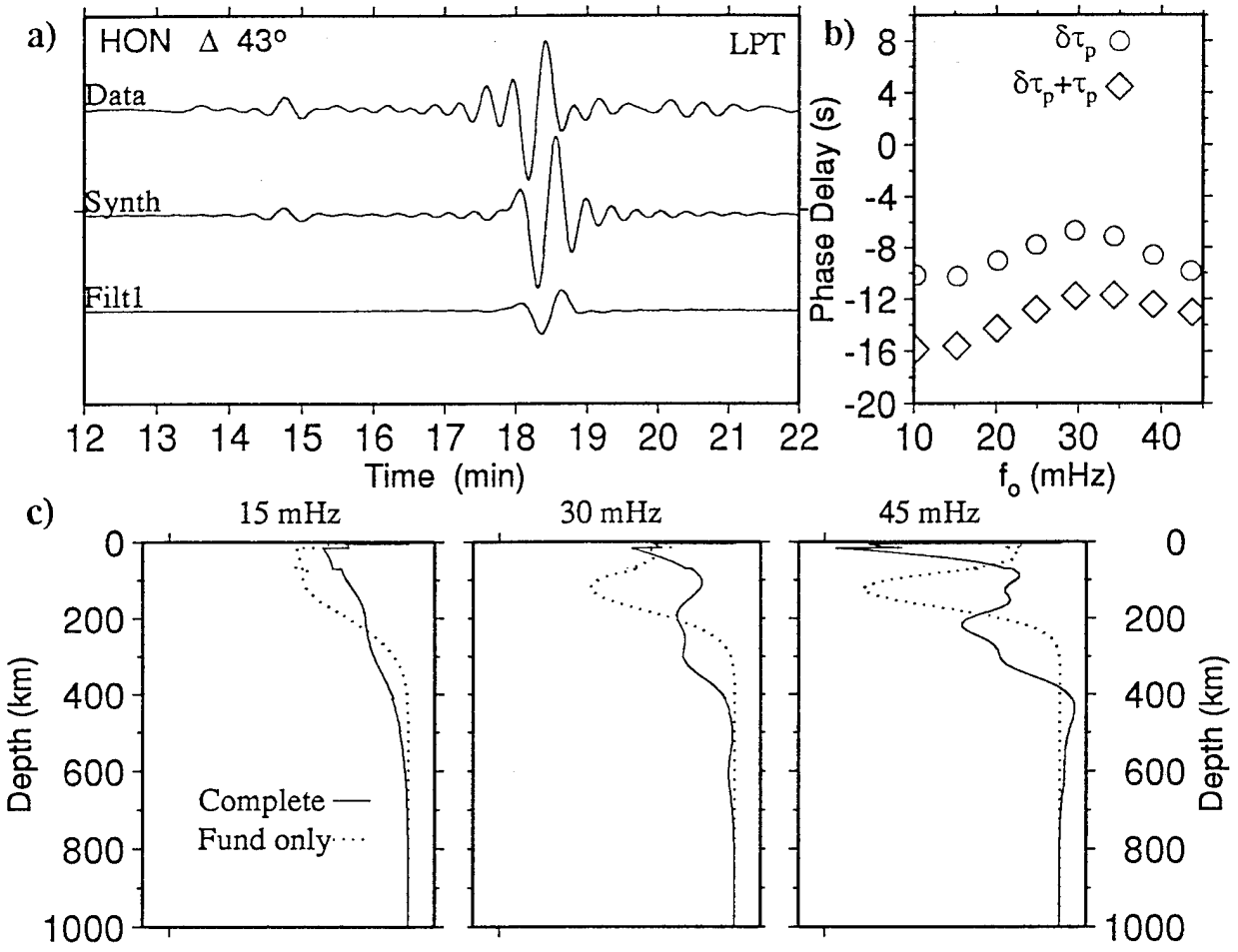

GMT Mar 10 14:59 pa3.ts 84111722 HON T fund

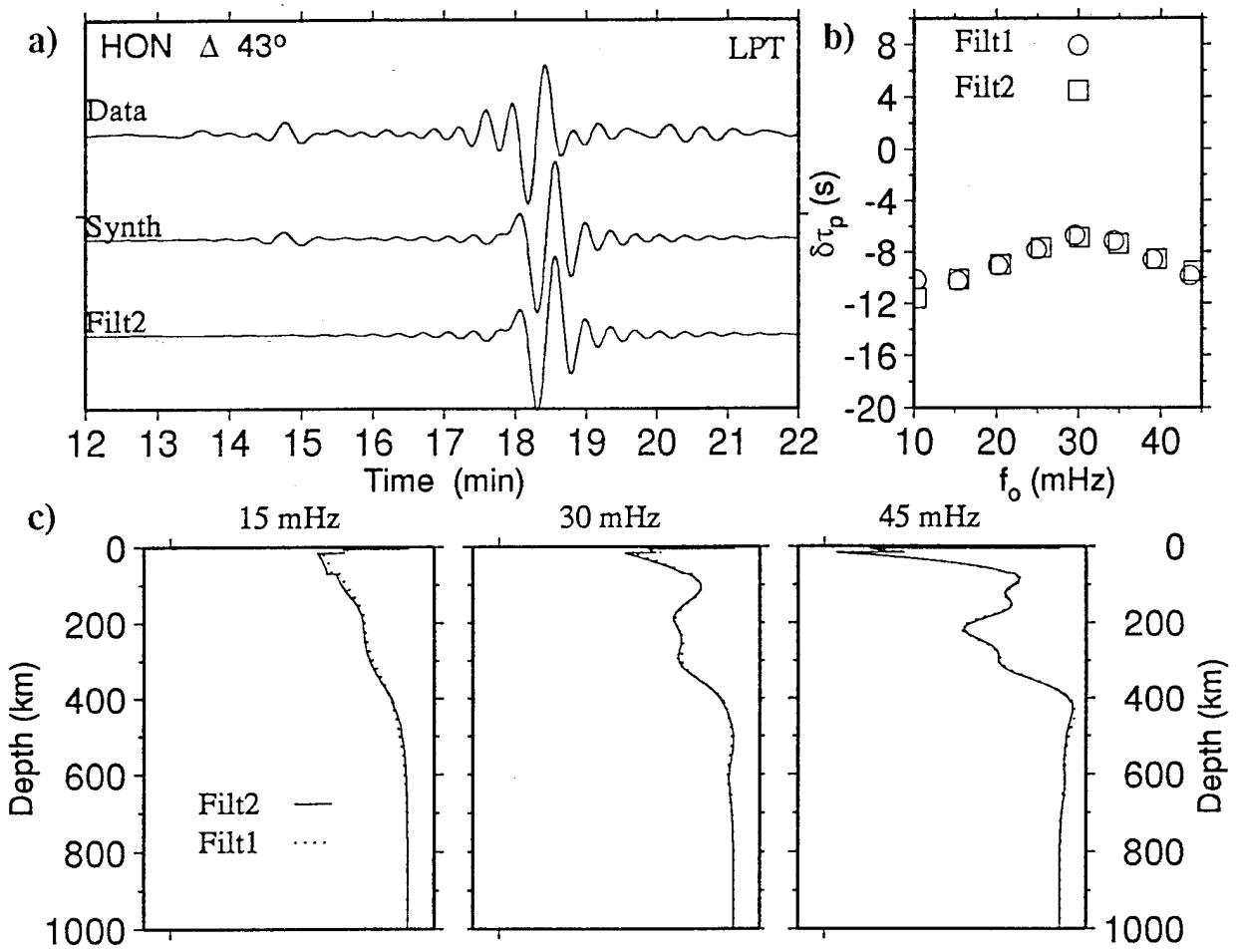
a)
HON Δ 43°
LPT
Data
Synth
Filt2
12 13 14 15 16 17 18 19 20 21 22
Time (min)
b)
Filt1
Filt2
8 4 0 -4 -8 -12 -16 -20
δτp (s)
10 20 30 40
fo (mHz)
c)
15 mHz
30 mHz
45 mHz
0 200 400 600 800 1000
Depth (km)
Filt2
Filt1

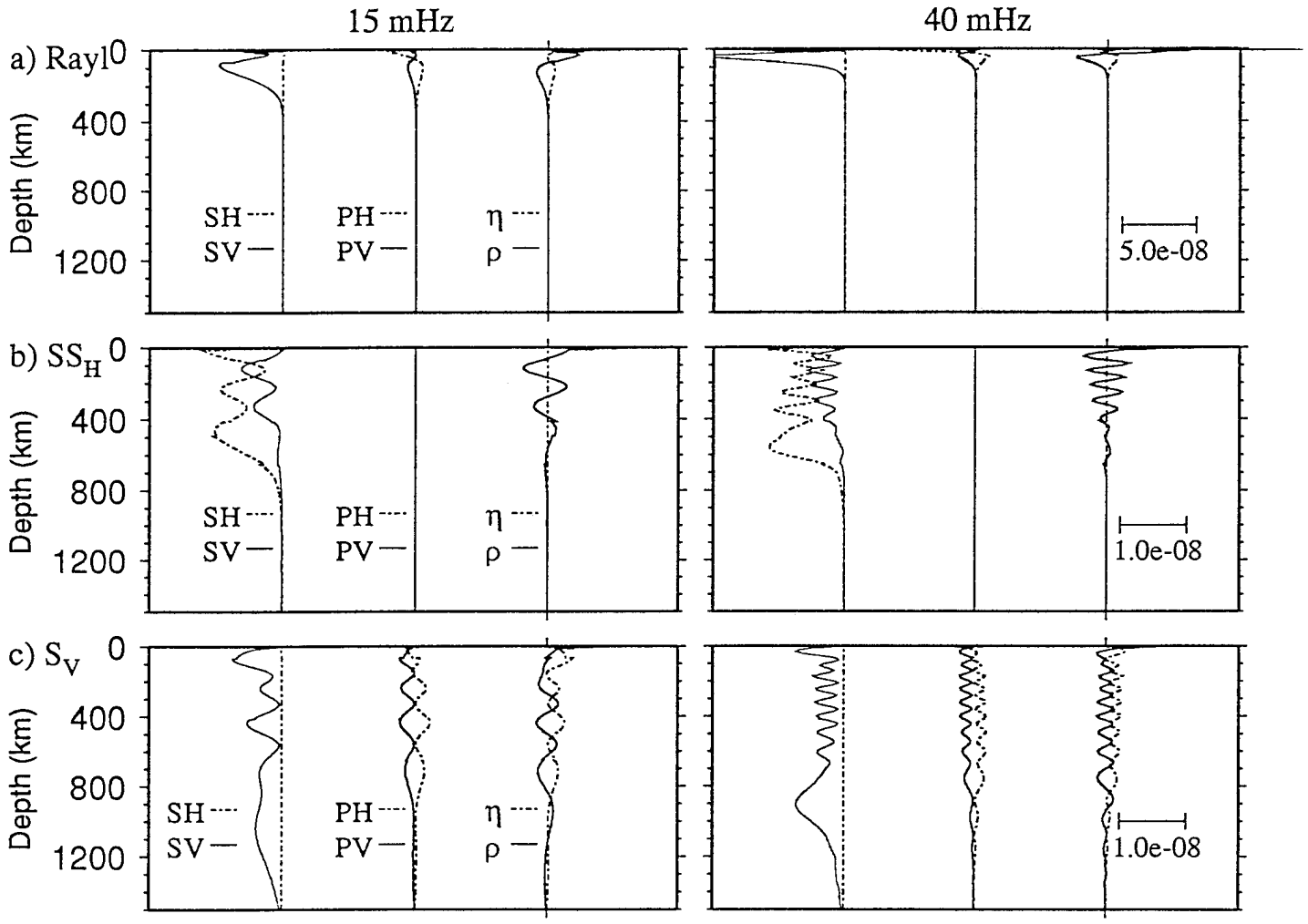

GMT Mar 20 15:44 pa4_3a 84111722 HON Z fund 87021000 HON T 4.69.02.8 87021000 HON Z 5.90.02.13

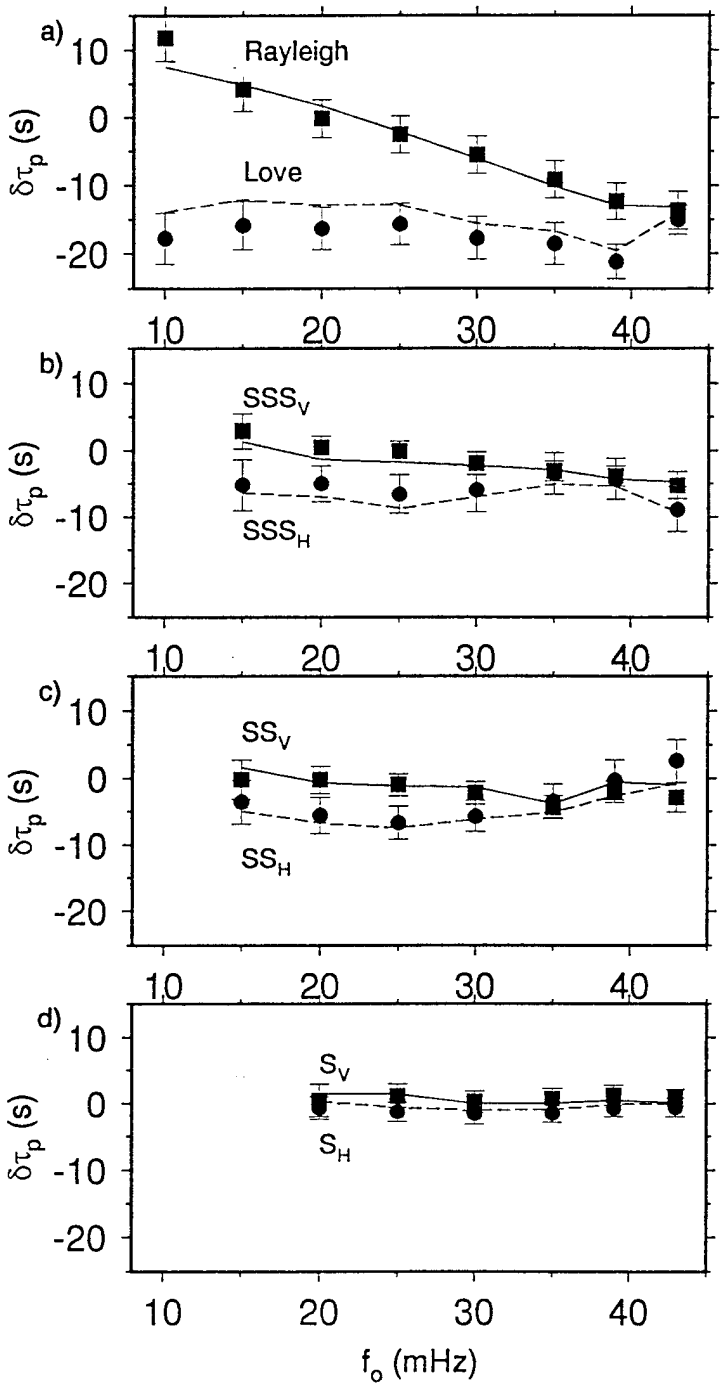
a)
Rayleigh
Love
b)
SSS$_V$
SSS$_H$
c)
SS$_V$
SS$_H$
d)
S$_V$
S$_H$
$\delta\tau_p$ (s)
10
0
-10
-20
10
20
30
40
f$_o$ (mHz)

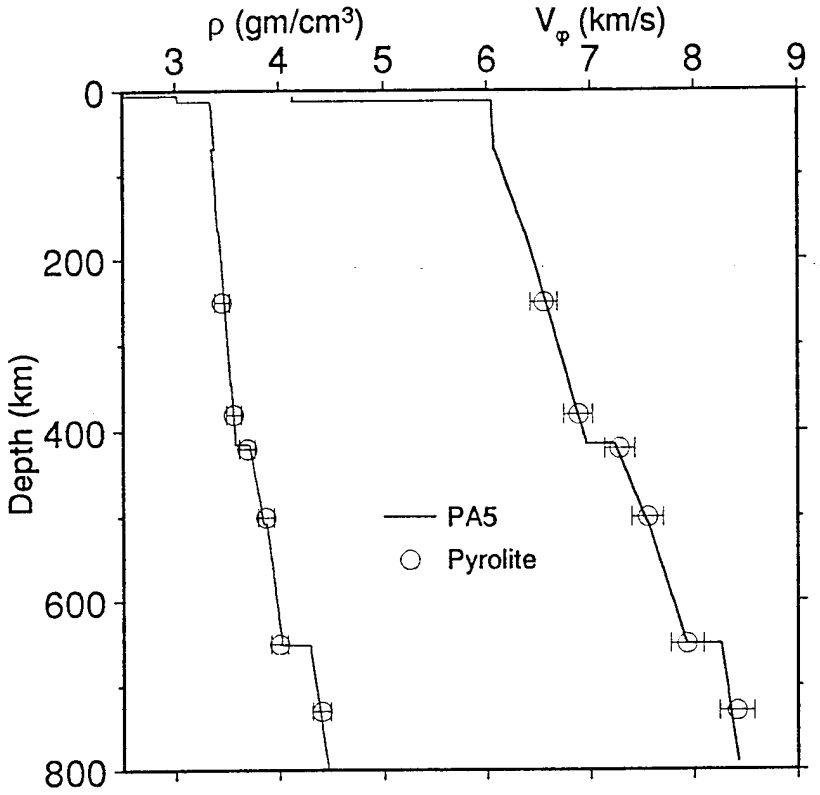
ρ (gm/cm³)
V_φ (km/s)
3
4
5
6
7
8
9
0
200
400
600
800
Depth (km)
PA5
Pyrolite

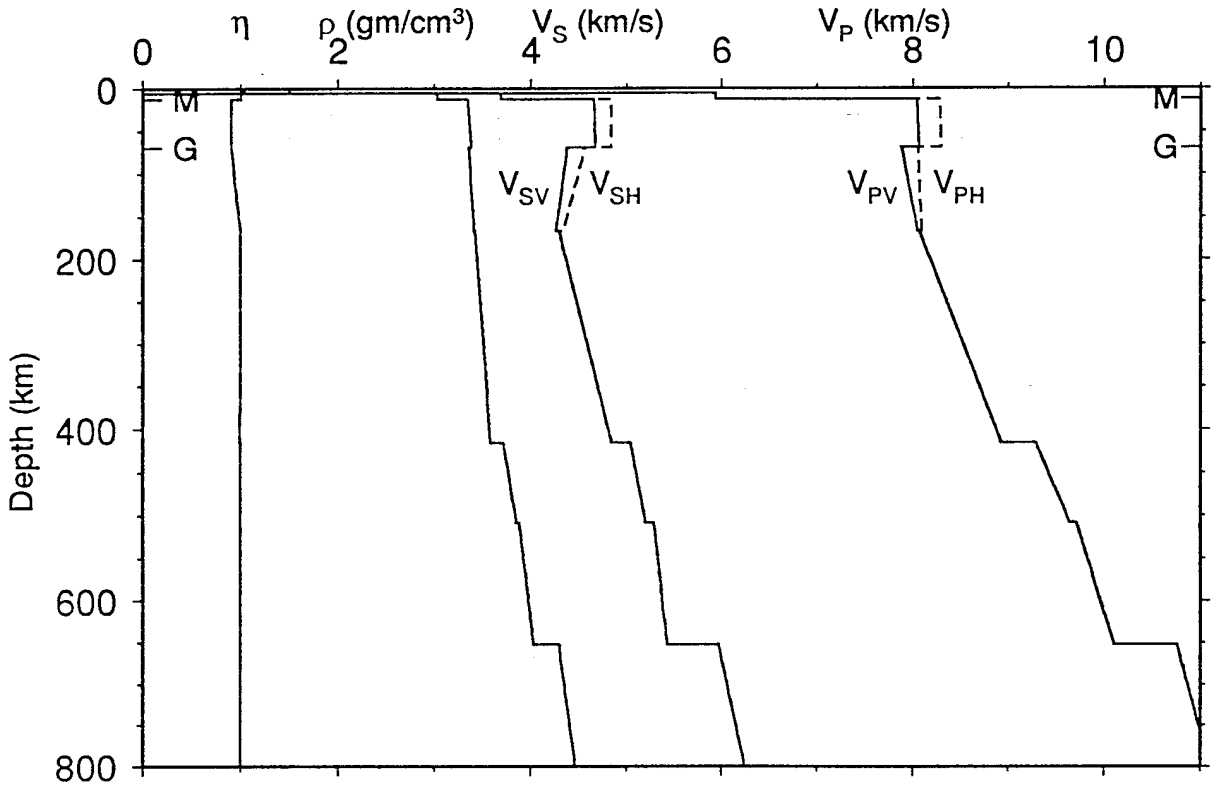
η
ρ (gm/cm³)
V_S (km/s)
V_P (km/s)
0
2
4
6
8
10
0
200
400
600
800
Depth (km)
M
G
V_{SV}
V_{SH}
V_{PV}
V_{PH}
M
G

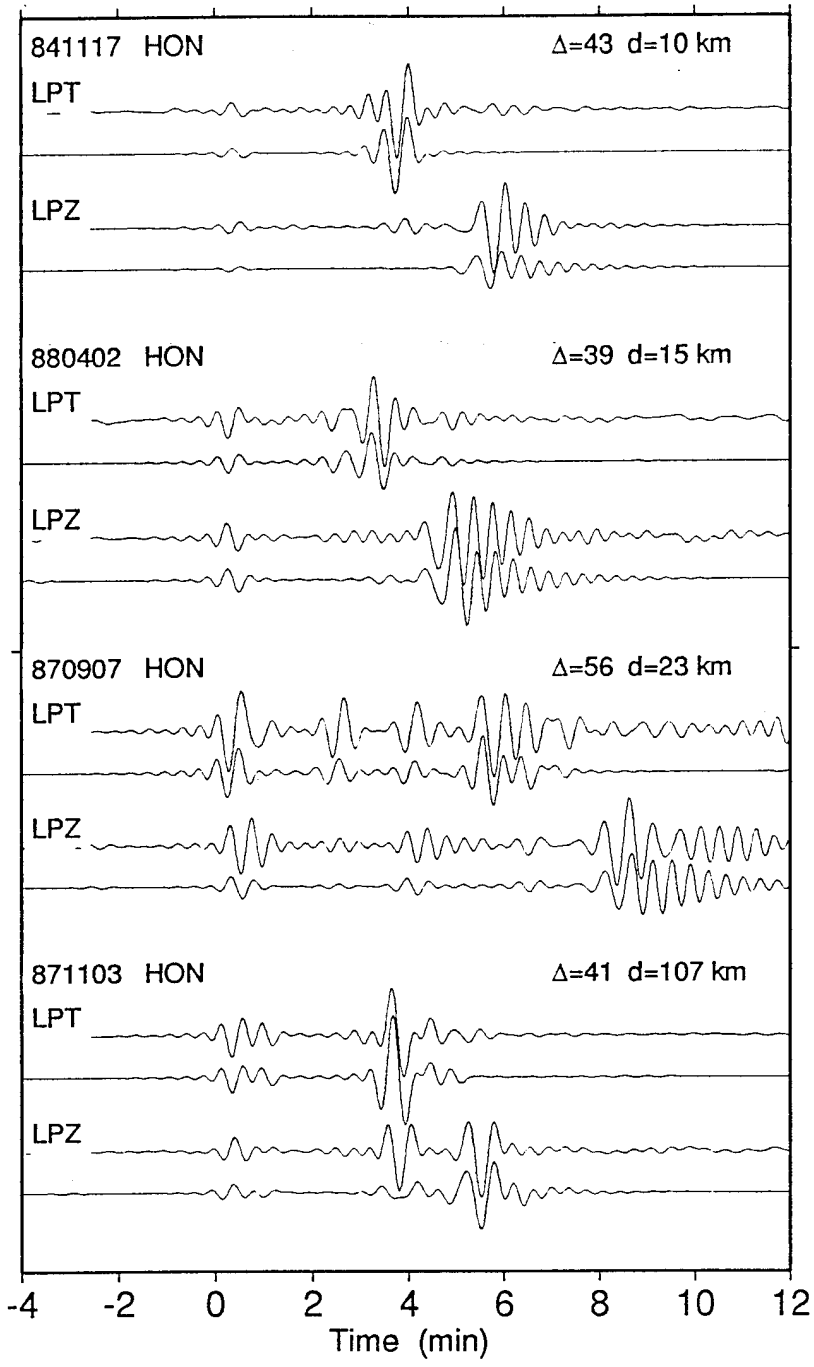
841117 HON
Δ=43 d=10 km
LPT
LPZ
880402 HON
Δ=39 d=15 km
LPT
LPZ
870907 HON
Δ=56 d=23 km
LPT
LPZ
871103 HON
Δ=41 d=107 km
LPT
LPZ
-4
-2
0
2
4
6
8
10
12
Time (min)

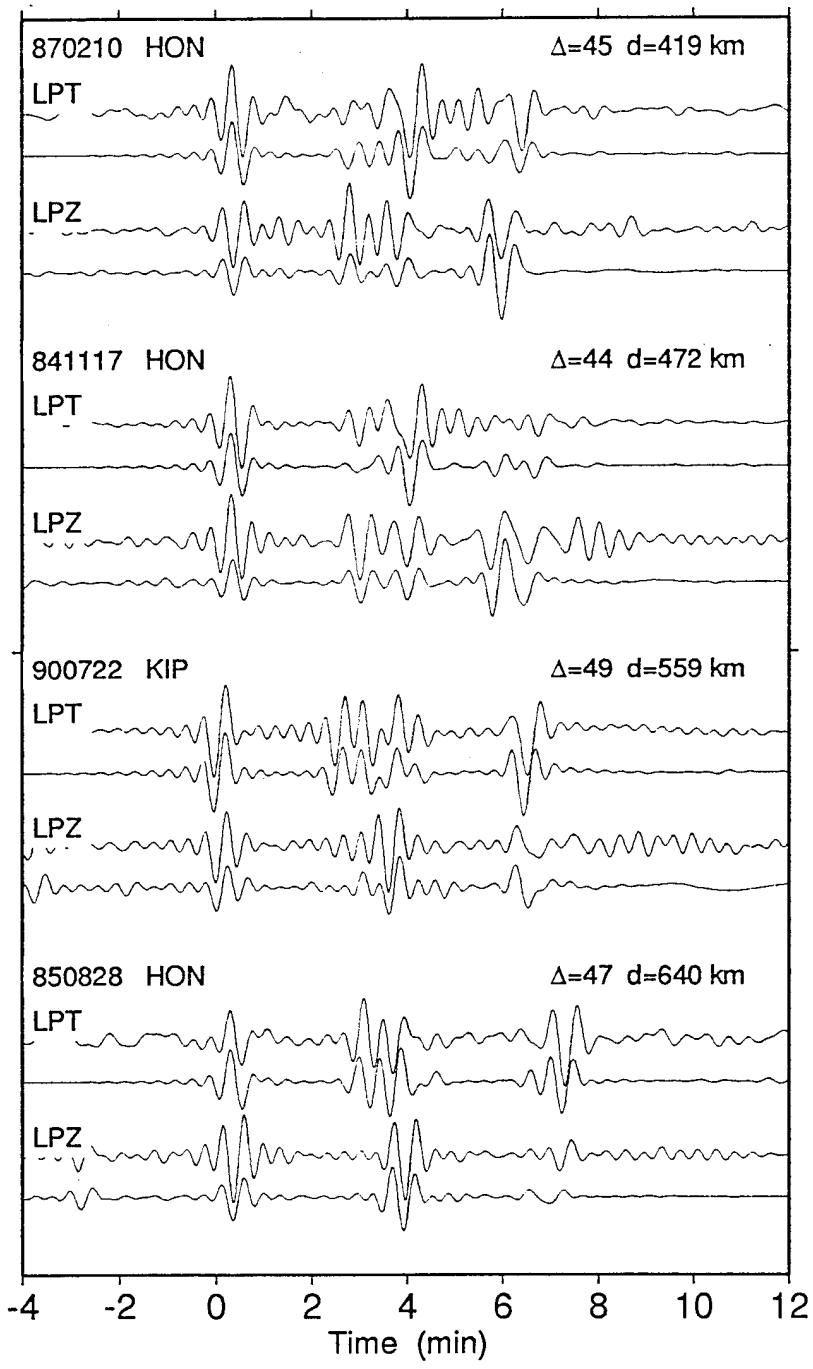
870210 HON
Δ=45 d=419 km
LPT
LPZ
841117 HON
Δ=44 d=472 km
LPT
LPZ
900722 KIP
Δ=49 d=559 km
LPT
LPZ
850828 HON
Δ=47 d=640 km
LPT
LPZ
-4
-2
0
2
4
6
8
10
12
Time (min)

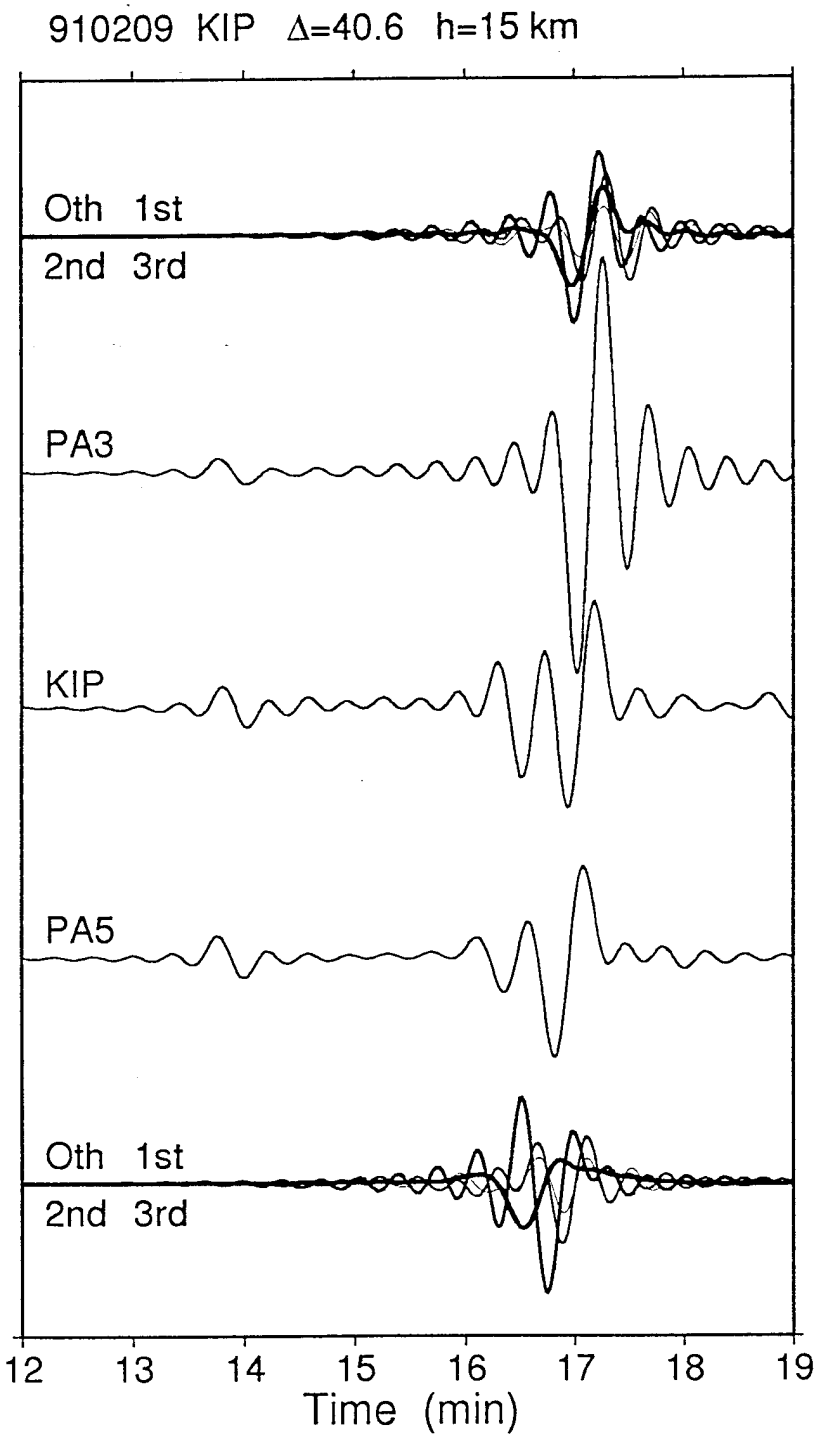
910209 KIP Δ=40.6 h=15 km
Oth 1st
2nd 3rd
PA3
KIP
PA5
Oth 1st
2nd 3rd
12
13
14
15
16
17
18
19
Time (min)

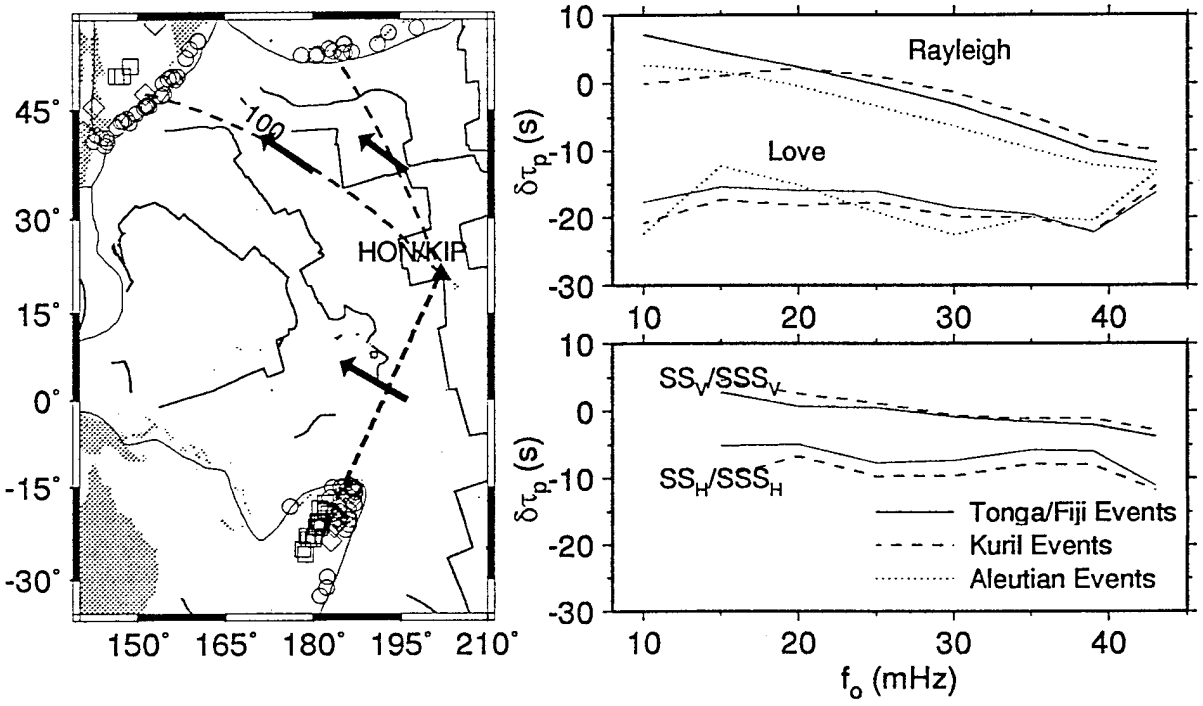
45°
30°
15°
0°
-15°
-30°
150°
165°
180°
195°
210°
-100
HONKIP
10
0
-10
-20
-30
Rayleigh
Love
δτp (s)
10
20
30
40
SSV/SSSV
SSH/SSSH
Tonga/Fiji Events
Kuril Events
Aleutian Events
fo (mHz)

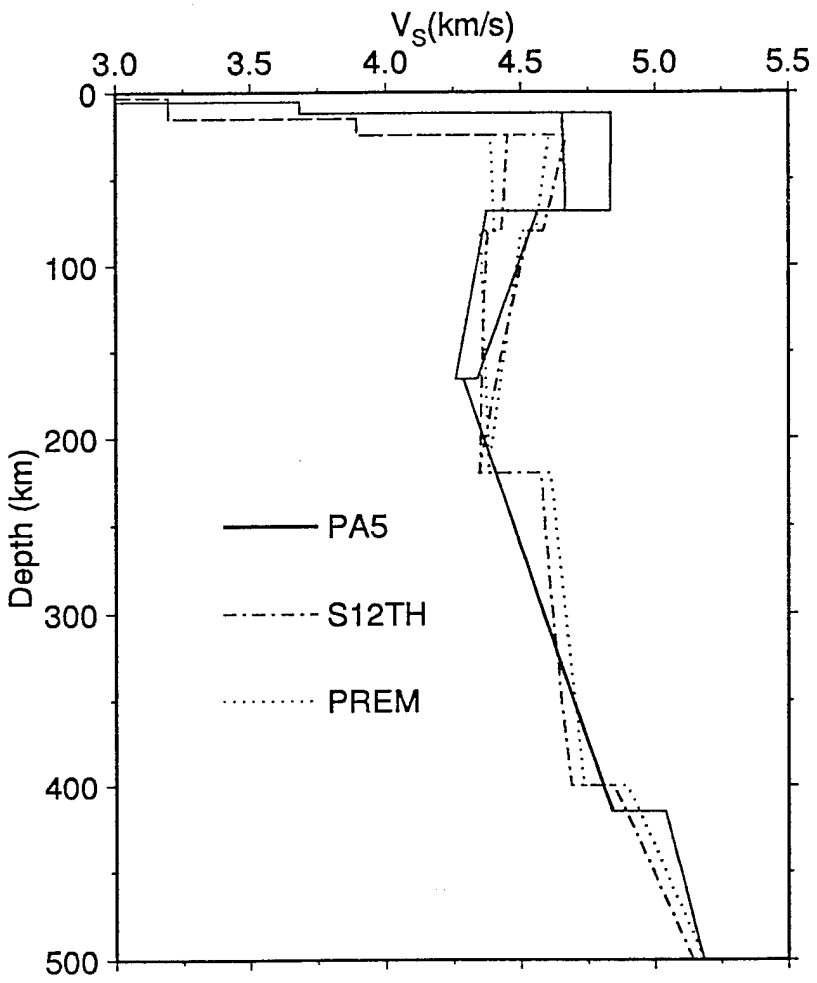
V_S(km/s)
3.0
3.5
4.0
4.5
5.0
5.5
0
100
200
300
400
500
Depth (km)
PA5
S12TH
PREM

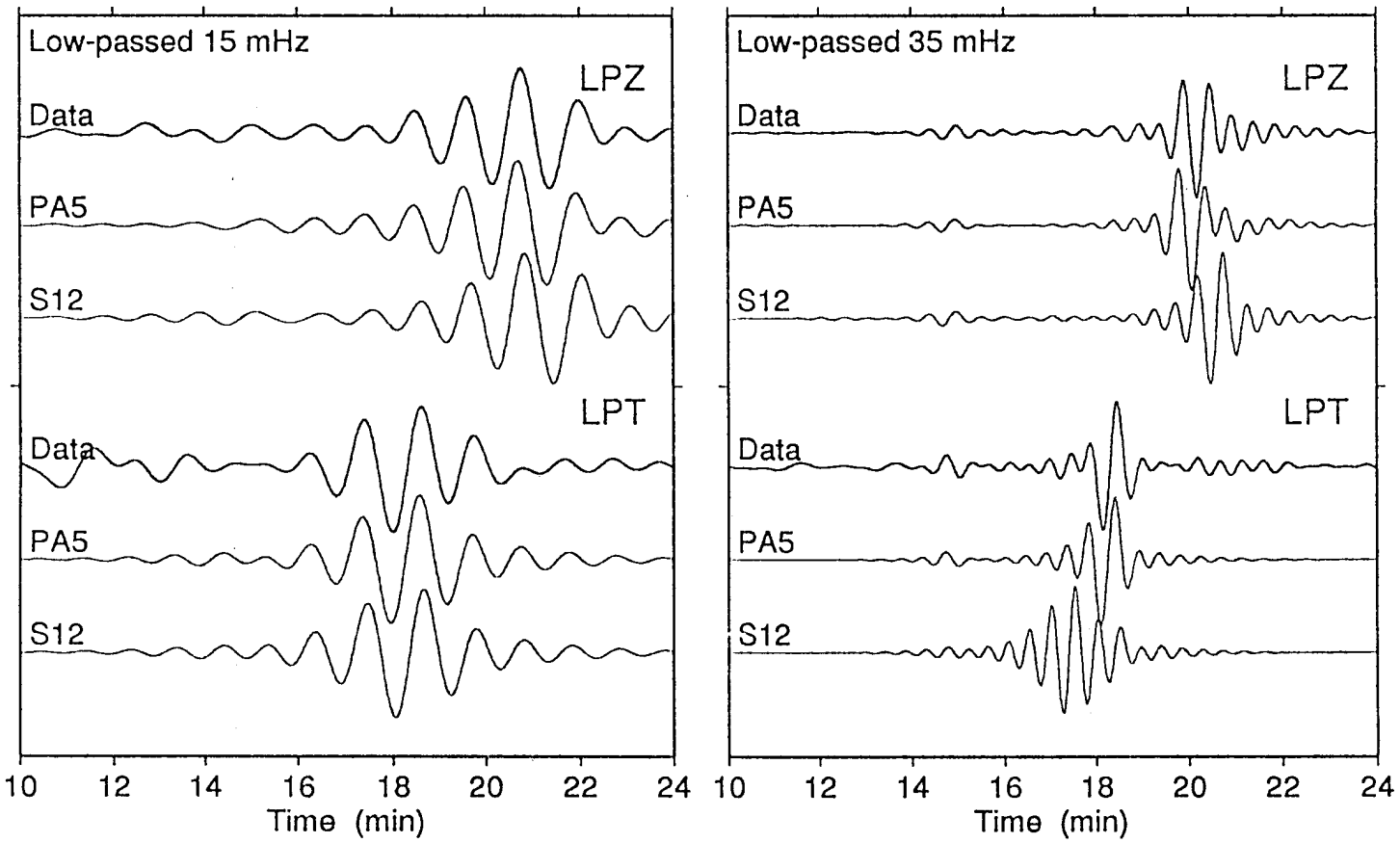
Low-passed 15 mHz
LPZ
Data
PA5
S12
LPT
Data
PA5
S12
10
12
14
16
18
20
22
24
Time (min)
Low-passed 35 mHz
LPZ
Data
PA5
S12
LPT
Data
PA5
S12
10
12
14
16
18
20
22
24
Time (min)